Large Mode Area Fibers of Multicore Type and Their Modal Properties

Diplomarbeit

FRIEDRICH-SCHILLER-UNIVERSITÄT JENA

PHYSIKALISCH-ASTRONOMISCHE FAKULTÄT

INSTITUT FÜR ANGEWANDTE OPTIK

eingereicht von

Christian Schulze

geboren am 29.06.1987 in Jena

1. Gutachter: Prof. Dr. rer. nat. habil. Richard Kowarschik

2. Gutachter: Dr. rer. nat. Michael Duparré

Tag der Verleihung des Diploms:

Contents

1 Introduction

Since the 1960s optical fibers gained evermore importance and are today well established in telecommunication, metrology and high power lasers [1]. In the last ten years a new type of fiber attracts attention: the multicore fiber (MCF) [2]. The main applications of MCFs include the generation of high brilliant beams (fiber lasers) [3], passive transport of light [4], measurement of strain and bends in form of fiber sensors [5], and enhancement of the transport capacity in optical network systems [6]. Such applications are established in the fields of laser material processing, medical engineering, and telecommunication.

Concerning the requirements of high optical power in laser material processing, MCF lasers represent a promising opportunity in scaling the output of fiber lasers to yet increasing power levels. The multiple cores of the MCF provide a larger total area compared to conventional step-index fibers [7], thus avoiding the onset of nonlinear effects which is an important condition in the active as well as the passive operation of the fiber. From the point of application, the fundamental mode of the fiber is mostly preferred because of its higher brightness and beam quality compared to higher order modes (HOMs). Various approaches exist to favor this mode, such as specifically designed feedback elements like external Talbot cavities [8], various types of fiber couplers [3] or mode selection via nonlinear processes [9]. However, distinct mode mixtures are also taken into consideration for enhancing the beam brilliance [10]. These efforts indicate the great significance, that is assigned to the modal composition.

Beside the modal content, a second important quantity is the polarization of the beam. Radially or azimuthally polarized light [11] can be used to increase the efficiency of material processing [12] or to focus light more tightly [13], which could be of interest in the field of medical engineering too. Thereby it is imaginable that more complex, optimized polarization distributions, adapted to special problems, could increase efficiencies even further.

Adjustment and control of modal content and polarization necessitate a fast and reliable measurement technique, as provided by the use of computer-generated holograms (CGHs) in combination with polarization analyzing elements. Whereas the measurement of the polarization is well established [14], measuring the modal content of a beam

constitutes a more challenging task. Known approaches contain the measurement of the Wigner distribution [15], numerical phase retrieval [16], the use of a ring-resonator [17], low-coherence interferometry [18], and spatially resolved spectral interferometry [19]. Whereas these techniques suffer from elaborate numerical calculations, limited applicability, or long measurement time, the striking advantage of the CGH-method is its real-time ability and the capability of measuring modal amplitudes and phases directly, without the need of sophisticated numerics.

Therefore, the main purpose of this work is to extend the CGH-technique for the investigation of MCFs with the demand on the complete description of the fields, i.e., including the polarization. The complete field characterization enables the examination of the modal properties of the fiber as a function of parameters such as the bending diameter, vertical pressure, excitation polarization and fiber length, providing deeper insight into the characteristics of the MCF. Thereby, the use of different excitation wavelengths allows the analysis of mode mixtures of different complexity and thus enhances the amount of available information.

The first part of this work adresses the calculation of modes in MCFs and their properties. Additionally, the measurement of the field and its polarization are theoretically described. The second part deals with the experimental determination of the number of modes, demonstrates the measurement of the complete field, and presents the behavior of the fiber while systematically varying the bending diameter, the amount of vertical pressure, the excitation polarization, and the fiber length. Subsequently, the decomposition of the MCF fields into step-index fiber LP (linearly polarized) modes and its merits, the beam quality and possibilities of its improvement as well as the Talbot effect are considered.

2 Theoretical Considerations

2.1 Multicore Fibers

Multicore fibers (MCFs) are optical fibers consisting of several high-index cylindrical cores embedded in a common cladding and thereby forming a waveguide array. In most cases the cores are arranged to build a hexagonal structure, but also rectangular or ringlike arrangements are investigated [20, 21].

One isolated core with the surrounding cladding behaves like a step-index fiber, whose physics is well-known [22]. Due to the existence of other cores in the neighborhood, the light propagation in one core is no longer unperturbed. A light wave propagating in one single core is influenced by the light in the other cores leading to waveguide coupling. Thereby it is clear that the waves in the cores are affected differently, because the number of next neighbor cores differs from core to core. The coupling is mostly caused by the overlap of the evanescent fields. But also other coupling mechanisms are reported [23]. The coupling of the individual cores leads to the formation of so-called "supermodes" that are described in more detail in the next section.

The MCF under investigation consists of 19 hexagonally arranged cores as depicted in fig. 2.1. The parameters specifying the geometry are the core-to-core distance $\Lambda = 5.5\,\mu\text{m}$ (pitch) and the core diameter $d = 2.2\,\mu\text{m}$. Together with the numerical aperture of the single cores NA = 0.108, or the index step from cladding to core[1] $\Delta n = n_{\text{co}} - n_{cl} = 4 \times 10^{-3}$, and the wavelength λ, the structure is completely defined (e.g., regarding the modal content) [4].

2.2 Calculation of Modes

For modal decomposition using computer-generated holograms (CGHs) it is necessary to know the propagating modes in the given structure of refractive index. Therefore this section is intended to introduce several concepts on how to calculate the modal patterns and the corresponding propagation constants.

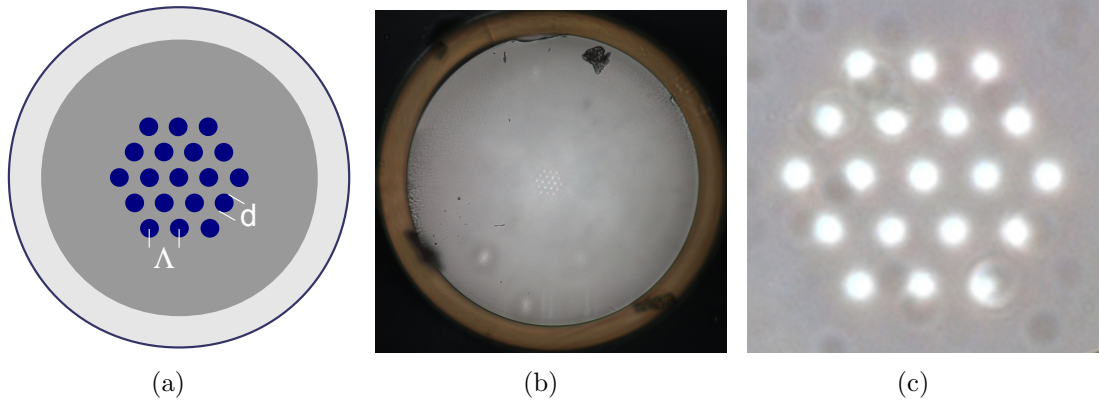[1]The material dispersion is neglected.

Fig. 2.1 (a) Schematic fiber cross section with geometry parameters Λ (pitch) and d (core diameter). (b) Microscope image of the front facet of the fiber. The outer brownish ring is the fiber coating. (c) Rotated and enlarged core area.

Basically there exist two different approaches for the calculation: the coupled mode theory (CMT) that relies on the mutual evanescent coupling between the individual cores of the fiber, and mode solvers that calculate the modes of the index structure as a whole, disregarding individual cores.

The modes in MCFs are sometimes called "supermodes" which is based on the fact that these modes are eigenstates of the entire structure whereas in general each single core has a modal distribution itself. But this term is only meaningful in the context of the CMT [7].

2.2.1 Coupled Mode Theory

In the CMT the index structure is regarded to consist of subdomains, namely the individual cores of the fiber, whose modes are assumed to be known since each core represents a step-index fiber itself. Usually, the individual cores are designed to be single-mode which simplifies calculation. The scalar field Ψ in the structure and its evolution during propagation in z-direction can be described by a superposition of the unperturbed fundamental modes $\mathcal{E}_l$ of the N cores ($l = 1 \ldots N$) weighted with a z-dependent amplitude $A_l(z)$ [9]:

$$\Psi(\boldsymbol{r}, z) = \sum_{l=1}^{N} A_l(z)\mathcal{E}_l(\boldsymbol{r}), \tag{2.1}$$

where $\boldsymbol{r} = (x, y)$, the transverse coordinates. The centerpiece of the CMT is the mutual interaction or coupling of each single core with all the other cores. The coupling is

represented in a set of differential equations for the amplitudes $A_l(z)$ [24]:

$$\frac{d\boldsymbol{A}_k}{dz} = i\widehat{\boldsymbol{C}}\boldsymbol{A}_k, \tag{2.2}$$

where $\widehat{\boldsymbol{C}}$ is the coupling matrix and $\boldsymbol{A}_k = [A_1 A_2...A_N]_k$, where k denotes the kth set of amplitudes describing the kth supermode. The z-invariance of the index structure justifies a harmonic z-dependence for the amplitudes $\boldsymbol{A}_k$. With the ansatz $\boldsymbol{A}_k = \boldsymbol{A}_k(0)e^{i\beta_k z}$, eq. (2.2) can be solved as an eigenvalue problem, where β_k is the propagation constant of the kth supermode. Therefore the solution of eq. (2.2) comprises N sets of vectors $\boldsymbol{A}_k(0)$ (each having $l = 1...N$ entries) and the corresponding β_k, that together characterize the N supermodes. According to the CMT, the number of supermodes is equal to the number of cores [24]. Since $\boldsymbol{A}_k(0)$ and β_k are known, the harmonic z-dependence allows the numerical propagation of a field consisting of an arbitrary superposition of the N supermodes.

To visualize the evanescent overlap of the fundamental modes of the individual cores $\mathcal{E}_l$, fig. 2.2(b) depicts the overlap integral in matrix form $M_{ij} = \iint \mathcal{E}_i \mathcal{E}_j dA$ and $M_{ij} = 0$, if $i = j$, for a wavelength of 633 nm, with the surface element dA, and integration over the whole transverse plane. The corresponding arrangement of cores is depicted in fig. 2.2(a). Since $M_{ij} = M_{ji}$, the matrix is symmetric. Further, the matrix reveals some symmetry properties as well as the number of next and higher order neighbors, that is denoted with N_1, N_2 etc., and the amount of overlap between them.

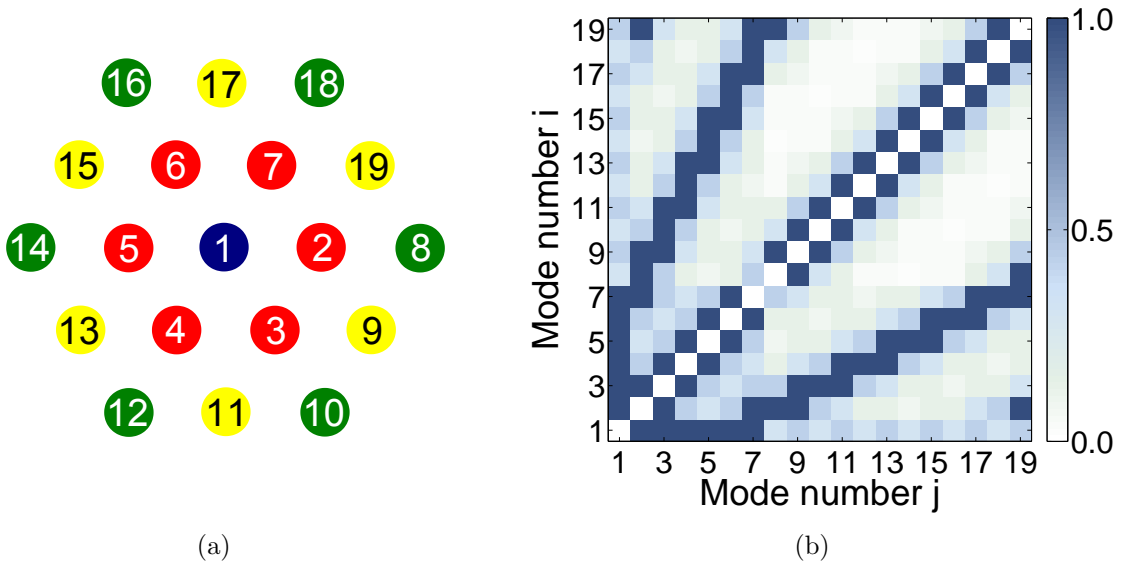(a)   (b)

Fig. 2.2 (a) Arrangement of cores. (b) Matrix M_{ij} describing the evanescent overlap of the fundamental modes in the individual cores at 633 nm (normalized to maximum value). Only the mutual interaction of fields is considered.

Consider for instance the line M_{1j} $(j = 1 \ldots 19)$ depicting the overlap of the central core (blue) to all others. It can be easily deduced that for this core $N_1 = N_2 = N_3 = 6$ with $\{N_1\} = 2, 3, 4, 5, 6, 7$, $\{N_2\} = 9, 11, 13, 15, 17, 19$ and $\{N_3\} = 8, 10, 12, 14, 16, 18$ (seen as long dark bar followed by an alternating pattern). Accordingly, the cores in the first ring (red) have $N_1 = 6$, $N_2 = 4$ and $N_3 = 3$, the ones in the corners of the second ring (green) $N_1 = 3$, $N_2 = 2$ and $N_3 = 3$ and the ones on the borders of the second ring $N_1 = 4$, $N_2 = 3$ and $N_3 = 2$.

The mutual overlap between next neighbors amounts to 46% of the power within one isolated core, between neighbors of second order 20%, and between neighbors of third order 14%. The corresponding distances are $s_{N1} = \Lambda$, $s_{N2} = \sqrt{3}\Lambda$ and $s_{N3} = 2\Lambda$.

The number of neighbors of different order, the distance to them and the overlap between them, are important quantities that determine the shape and symmetry of the supermodes.

The ansatz of the CMT is true in the regime of weak coupling of neighboring cores. Therefore, results become incorrect at longer wavelengths as will be discussed in sec. 2.3.1.

2.2.2 Vectorial Mode Solvers

In contrast to the CMT, there are mode solvers calculating modes from index profiles that need not to contain individual waveguides. Two kinds of mode solvers shall be introduced in the following. First, there are mode solvers handling arbitrary index profiles. These usually solve an eigenvalue problem resulting from Maxwells equations, with the advantage of utmost generality and applicability. Another approach is to make use of specific symmetries of the problem to reduce computational effort. The advantage of faster computation is therefore accompanied with the restriction to a smaller class of problems that can be solved.

Note that in this new context the term "supermode" becomes meaningless and is simply replaced by "mode" unless there are reasons for confusion.

Mode Solvers Rigorously Solving Maxwells Equations

Maxwells equations[2] and translation invariance in z (all field components $\propto e^{i\beta z}$) can be used to deduce an eigenvalue problem for the transverse magnetic field $\boldsymbol{H}_t$ [25]:

$$\nabla_t^2 \boldsymbol{H}_t(\boldsymbol{r}) + \frac{\omega^2}{c^2}\varepsilon(\boldsymbol{r})\boldsymbol{H}_t(\boldsymbol{r}) + \nabla_t \ln \varepsilon \times \nabla_t \times \boldsymbol{H}_t(\boldsymbol{r}) = \beta^2 \boldsymbol{H}_t(\boldsymbol{r}). \qquad (2.3)$$

---

[2]The material is assumed to be non-magnetic, isotropic and without free charges or currents.

with $\nabla_t = [\partial_x\, \partial_y\, 0]'$, $\varepsilon(\boldsymbol{r})$ the permittivity distribution, ω the angular frequency, β the eigenvalue and c the velocity of light.

The z-component of the magnetic field vector follows from $\nabla \cdot \boldsymbol{H} = 0$:

$$H_z = \frac{1}{i\beta}\nabla_t \cdot \boldsymbol{H}_t(\boldsymbol{r}). \tag{2.4}$$

The electric field vector can be calculated from $\boldsymbol{H}$:

$$\boldsymbol{E}(\boldsymbol{r}) = \frac{i}{\omega\varepsilon_0\varepsilon(\boldsymbol{r})}\nabla \times \boldsymbol{H}(\boldsymbol{r}). \tag{2.5}$$

with $\nabla = [\partial_x\, \partial_y\, \partial_z]'$ and ε_0 the permittivity of vacuum.

It is also possible to derive an eigenvalue problem for the transverse components of the electric field. But then, the operator of the resulting eigenvalue problem is no longer Hermitian. Note that in both cases two of six field components are sufficient to build the solution. A simplification arises if $\varepsilon(\boldsymbol{r})$ is piecewise uniform and the index difference between core and cladding is small. In this case $\nabla_t \ln \varepsilon(\boldsymbol{r}) \approx 0$ and the transverse components of the magnetic field in eq. (2.3) are decoupled to form the Helmholtz equation [25]:

$$\left[\nabla_t^2 + \frac{\omega^2}{c^2}\varepsilon(\boldsymbol{r})\right]\boldsymbol{H}_t(\boldsymbol{r}) = \beta^2\boldsymbol{H}_t(\boldsymbol{r}) \tag{2.6}$$

Numerical solving schemes for eq. (2.3) as well as eq. (2.6) are for example finite difference methods (FD) [26, 27], finite element methods (FEM) [28] as used by COMSOL Multiphysics® (COMSOL), and the source model technique (SMT) [29].

Mode Solvers Exploiting Cylindrical Symmetry

An approach that is used for geometries with cylindrical symmetry is the multipole method as described in [30, 31]. The method is applicable for every structure that consists of periodically arranged inclusions in a background material. The fields are expanded in Fourier-Bessel series, i.e., in terms of Bessel and Hankel functions that form a natural basis in cylindrical coordinates. The solution then comprises a set of Fourier-Bessel coefficients. The free simulation tools of CUDOS MOF (CUDOS) are used to apply this technique.

There are several extensions of the method to enable the calculation of index structures with non-cylindrical inclusions [32].

2.2.3 The Effective Step-index Model

The modes of step-index fibers are well known and can be described by analytic formula [22]. Therefore it can be desirable to replace the complicated structure of MOFs with an equivalent step-index (ESI) structure. In the case of MCFs the task is to find an appropriate core index. This is done by calculating the effective index of the fundamental space-filling mode (FSM) [33], which is the mode of the infinite hexagonal array of cores, or its elementary cell, with the highest effective index. In this work this index was calculated using a FD approach. The equivalent core radius can be computed analytically as described in [33].

At short wavelengths the description of the MCF with the ESI model is restricted, since the number of modes in the MCF cannot exceed 19 (cf. sec. 2.2.1), whereas for a step-index fiber the number of modes is continuously growing with decreasing wavelength.

2.2.4 Comparison and Results

In this section the modal fields of the MCF under investigation will be presented as well as a comparison between the mode fields and the corresponding propagation constants calculated with different numerical mode solvers.

Fig. 2.3 depicts the fields of all 19 exciteable modes as computed with the scalar CMT at 633 nm. This wavelength is chosen to provide sufficient weak coupling to justify the ansatz of the CMT. It is important to note that at 633 nm only the first 12 modes are propagating ($n_{\text{eff}} > n_{\text{cl}}$), where this number is dependent on wavelength. Additionally, the modal fields and the corresponding propagation constants slightly change with wavelength, but the shape of the modes stays basically the same (see sec. 2.3.1). The results obtained using different mode solvers are compared in tab. 2.1. Thereby the calculated effective mode indices and the overlap integral of the modal fields serve as comparative values. The results obtained with COMSOL are chosen as reference, since this software is widely used and commercially available. For the vectorial solvers the H_x-component of the field was chosen to compare the fields. Examining the mode indices, the results obtained with CUDOS agree best, whereas the CMT yields slightly less exact results. The accordance regarding the values of the overlap integrals is very high for all mode solvers. Most according mode fields are obtained by CUDOS and the SMT with mean overlap exceeding 99.9 %. Further, the high agreement of $> 99\,\%$ demonstrate the reliability of the CMT approach. The results of the ESI model show the largest discrepancy to the reference. But considering that here the calculation is based on a different index structure, the agreement is more than satisfying.

In contrast to the other mode solvers the accuracy of the CMT approach drops with increased wavelength [7], which becomes apparent in $\Delta n_{\text{eff}}^{\text{cmt}} = 2 \times 10^{-4}$ and $I_{\text{cmt}} = 88.84\,\%$ for the fundamental mode at 1064 nm.
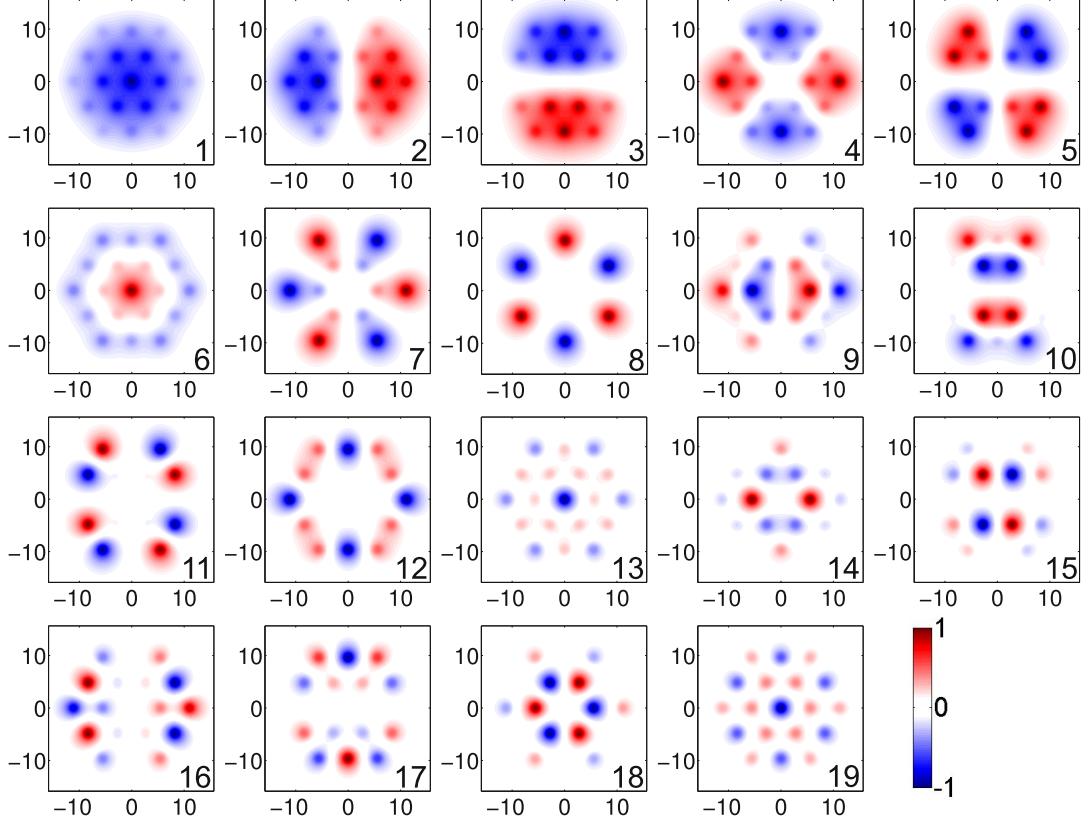

Fig. 2.3 Normalized modal fields of the MCF calculated with the CMT at 633 nm, arranged according to their effective indices (axes dimensions in µm).

$n_{\text{eff}}^{\text{fem}}$	$\Delta n_{\text{eff}}^{\text{cmt}}$	$\Delta n_{\text{eff}}^{\text{fd}}$	$\Delta n_{\text{eff}}^{\text{cud}}$	$\Delta n_{\text{eff}}^{\text{smt}}$	$\Delta n_{\text{eff}}^{\text{esi}}$	I_{cmt} [%]	I_{fd} [%]	I_{cud} [%]	I_{smt} [%]	I_{esi} [%]
1.45063515	7e-5	5e-6	6e-9	4e-6	1e-5	98.96	99.96	99.97	99.97	97.45
1.45051956	4e-5	1e-6	2e-9	3e-6	3e-5	99.14	99.95	99.97	99.95	97.00
1.45051951	4e-5	6e-6	5e-9	4e-6	3e-5	99.13	99.95	99.99	99.97	96.99
1.45037293	6e-6	3e-7	6e-9	5e-6	7e-5	99.70	99.67	99.98	99.92	96.04
1.45037292	7e-6	2e-6	1e-8	5e-6	7e-5	99.61	99.84	99.89	99.93	95.94
1.45032269	1e-6	5e-6	2e-8	6e-6	7e-5	99.83	99.66	99.96	99.90	95.83
	3e-5	3e-6	8e-9	5e-6	5e-5	99.39	99.84	99.96	99.94	96.54

Tab. 2.1 Comparison of effective mode indices and mode fields at 633 nm for mode 1 to 6 with $\Delta n_{\text{eff}}^{\text{x}} = |n_{\text{eff}}^{\text{fem}} - n_{\text{eff}}^{\text{x}}|$ and $I_{\text{x}} = \iint \Psi_{\text{fem}}^* \Psi_{\text{x}} dA$, the overlap integral with the appropriate field component Ψ. The last row depicts the mean values of the column above. Abbreviations as stated before.

2.3 Properties of Modes

2.3.1 Number and Shape

The number of modes is defined in this work as the number of propagating modes with different modal patterns. According to the CMT, a MCF with 19 cores will have 19 excitable modes as depicted in fig. 2.3. Some of these modes are propagating ($n_{\text{eff}} > n_{\text{cl}}$), the others are radiating ($n_{\text{eff}} < n_{\text{cl}}$). For modal decomposition only the propagating modes are of interest, because the investigated fiber lengths are sufficiently large. The number of propagating modes depends on the wavelength of the input light and on fiber parameters such as core diameter, pitch and index distribution.

Fig. 2.4, depicting the number of modes calculated with the FD solver, demonstrates, the larger the wavelength the smaller the number of propagating modes.
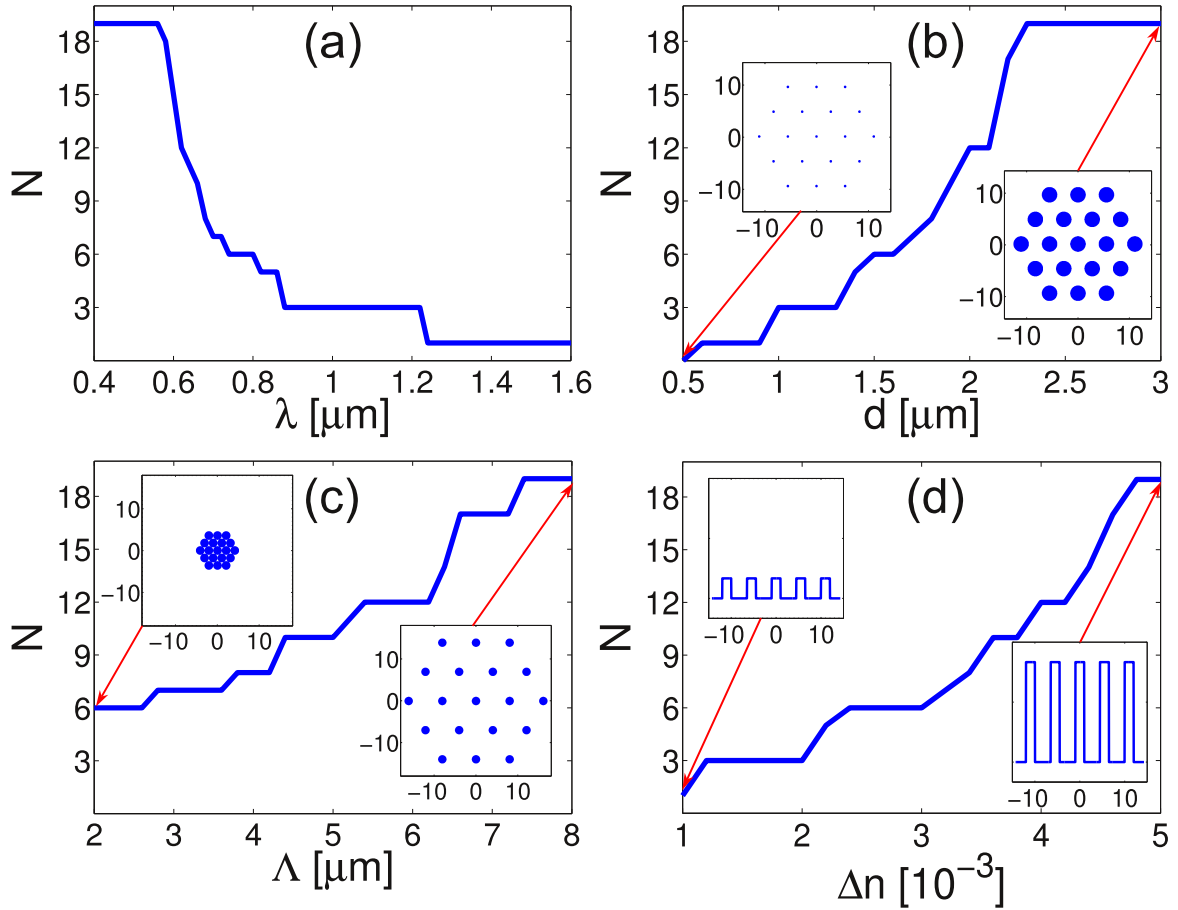

Fig. 2.4 Number N of modes depending on wavelength λ (a), core diameter d (b), pitch Λ (c) and index step Δn (d). The not varied structural parameters are those described in sec. 2.1. For (b)-(d) the chosen wavelength is 633 nm. The insets (units in µm) visualize the geometry of the fiber cross section ((b),(c)) and a slice through the index distribution (d). Calculations done with the FD solver.

Analogously, the number of such modes becomes smaller with decreasing core diameter, with decreasing pitch or with decreasing index step from core to cladding. This behavior is easily explained by considering the extension of the field of a single core into the cladding. Obviously, the number of modes decreases the weaker the light is guided in the cores and the larger the evanescent fields overlap. Fig. 2.5 exemplarily shows, on the basis of the respective fundamental modes, that an increasing wavelength leads to a decreasing total power fraction in the cores. Therefore it is true that the stronger the coupling between cores the less modes propagate. This can be understood as an increasing synchronization of phases or as phase locking, leading to the in-phase supermode for very strong coupling.

The number of modes at the investigation wavelengths 633 nm, 780 nm and 1064 nm is twelve, six and three due to calculation. Note that the limitation to 19 modes, as predicted by the CMT, is reproduced by the FD solver as well.
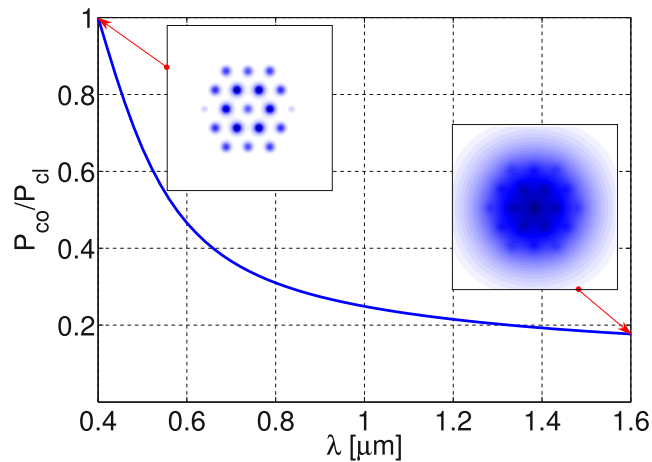

Fig. 2.5 Normalized ratio of total power in the cores to total power in the cladding as a function of wavelength on the basis of the respective fundamental modes. The insets depict the corresponding mode fields at 400 nm and 1600 nm.

2.3.2 Polarization State

Numerically solving eq. (2.6) on page 7 for the structure of the investigated fiber yields modes with distinct polarization properties. First, for each mode exists a dominating transverse component in $\boldsymbol{E}$ or $\boldsymbol{H}$. This characteristic is demonstrated in fig. 2.6 for the fundamental mode at 1064 nm, where the dominating components are H_y and E_x. Regarding all modes, the power ratio of the weak to the dominant transverse component varies in-between $6 \times 10^{-9} \ldots 8 \times 10^{-5}$ at 1064 nm, and $2 \times 10^{-8} \ldots 2 \times 10^{-3}$ at 633 nm. Second, the modes are nearly transverse, i.e., the z-component of the electric field E_z or

magnetic field H_z is very small compared to the dominating transverse component (see fig. 2.6). The power ratio of the z-component with respect to the dominating transverse component varies in-between[3] $(1\ldots 4)\times 10^{-4}$ at 1064 nm, and $(3\ldots 9)\times 10^{-4}$ at 633 nm. Thus, the modes are linearly polarized in good approximation in either x- or y-direction.
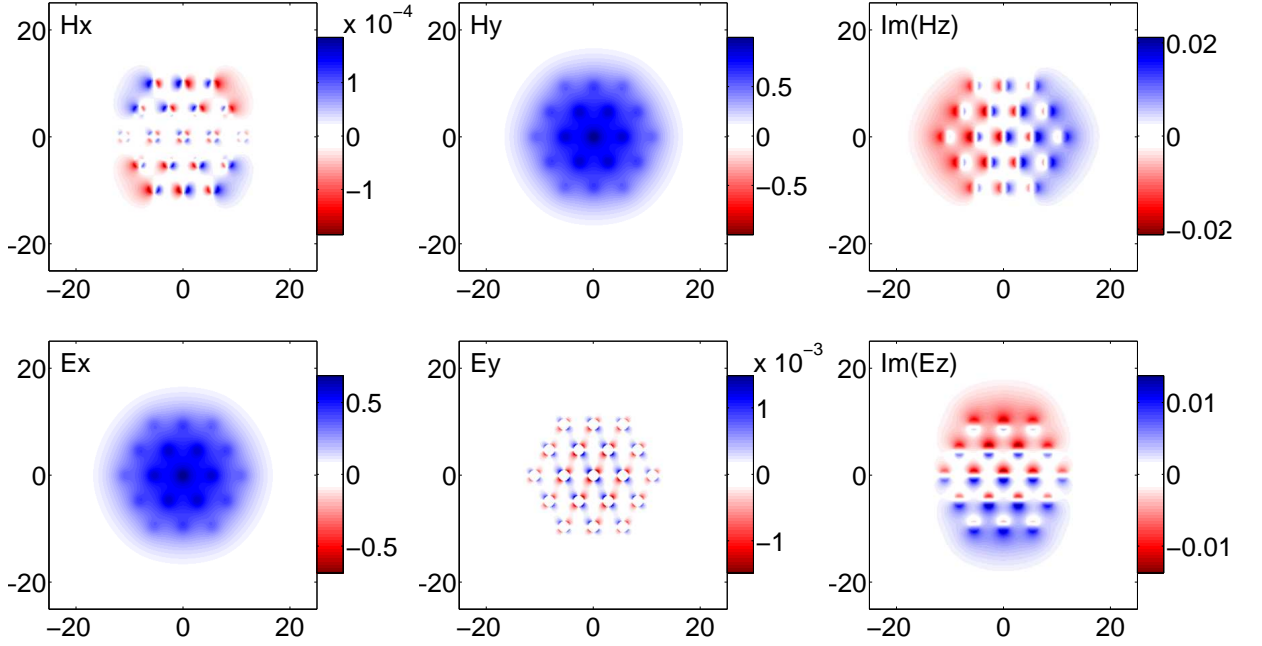

Fig. 2.6 Field components of the fundamental mode at 1064 nm. The dominating component is H_y with power P_{H_y}. The power of the remaining fields amounts to $P_{H_x} = 5.7 \times 10^{-9} P_{H_y}$, $P_{H_z} = 1.4 \times 10^{-4} P_{H_y}$, $P_{E_x} = 4.8 \times 10^{-1} P_{H_y}$, $P_{E_y} = 1.9 \times 10^{-7} P_{H_y}$ and $P_{E_z} = 6.7 \times 10^{-5} P_{H_y}$.

2.3.3 Orthogonality and Completeness

Emanating from the reciprocity theorem for Maxwells equations, a general orthogonality relation for optical waveguide modes can be established [34]:

$$\iint \left(\boldsymbol{E}_i^* \times \boldsymbol{H}_j \right) \cdot \boldsymbol{e}_z dA = \iint \left(E_{ix}^* H_{jy} - E_{iy}^* H_{jx} \right) dA = \delta_{ij}, \qquad (2.7)$$

where $\boldsymbol{e}_z$ is the unit vector in z-direction, dA is the surface element and δ_{ij} the Kronecker symbol. The integration is performed over the whole transverse plane.

Since the modes in the MCF are approximately linearly polarized (see sec. 2.3.2), there exists a coordinate system for each mode such that one of the transverse components E_x or E_y and H_x or H_y, respectively, is approximately zero. Therefore the orthogonality

---

[3]The given values are valid for $\boldsymbol{E}$ and $\boldsymbol{H}$

relation of eq. (2.7) can be written in scalar form:

$$\iint \Psi_i^* \Psi_j \, dA = \delta_{ij},$$ (2.8)

with Ψ representing the appropriate field component.

The discrete orthogonal modes build a complete set and hence, every field $\boldsymbol{U}(\boldsymbol{r})$ can be decomposed:

$$\boldsymbol{U}(\boldsymbol{r}) = \sum_{l=1}^{2N} c_l \boldsymbol{\Psi}_l(\boldsymbol{r}) = \sum_{l=1}^{2N} c_l \Psi_l(\boldsymbol{r}) \boldsymbol{e}_l,$$ (2.9)

with $c_l = \varrho_l e^{i\varphi_l}$ the complex expansion coefficient and $\boldsymbol{\Psi}_l(\boldsymbol{r}) = \Psi(\boldsymbol{r}) \boldsymbol{e}_l$ the lth mode with amplitude ϱ_l and *inter*modal phase φ_l (with respect to a reference phase). The latter formulation in eq. (2.9) splits the vector field into two factors: $\Psi_l(\boldsymbol{r})$ representing the field distribution and $\boldsymbol{e}_l$ a unit vector containing the polarization of the lth mode. Note that $\boldsymbol{e}_l$ is not spatially dependent since a mode is globally linearly polarized. Locally varying polarization is therefore a feature of vector fields composed of several modes.

The expansion (2.9) is valid as long as the radiation modes are negligible, which is the case in all experiments of this work.

2.4 Field Decomposition into a Composite Set of Modes

As shown in sec. 2.3.2, each mode is approximately linearly polarized. But there is a polarization degeneracy meaning that each mode occurs twice[4] with two orthogonal polarization states. Since the refractive index profile is rather hexagonal than of cylindrical symmetry, these modes propagate with different propagation constants (or effective indices) in the fiber and their mode field distribution will be slightly different. This difference is negligible ($\Delta n_{\text{eff}} \approx 10^{-8}$) because of the weak guidance of the investigated fiber and therefore it is reasonable to summarize the respective modes as field components to one vector mode with two non-vanishing transverse components:

$$\boldsymbol{U}(\boldsymbol{r}) = \sum_{l=1}^{2N} c_l \Psi_l(\boldsymbol{r}) \boldsymbol{e}_l = \sum_{g=1}^{2} \sum_{k=1}^{N} c_{kg} \Psi_{kg}(\boldsymbol{r}) \boldsymbol{e}_{kg} = \sum_{k=1}^{N} \left(c_{k1} \Psi_{k1}(\boldsymbol{r}) \boldsymbol{e}_{k1} + c_{k2} \Psi_{k2}(\boldsymbol{r}) \boldsymbol{e}_{k2} \right).$$ (2.10)

---

[4]"Twice" refers to the fact that the intensity patterns of two polarization degenerated modes are equal.

With the approximation $\Psi_{k1} \approx \Psi_{k2} = \Psi_k$ (quasi polarization degeneracy) it follows:

$$\boldsymbol{U}(\boldsymbol{r}) = \sum_{k=1}^{N} \Psi_k(\boldsymbol{r}) \begin{bmatrix} \varrho_{kx}e^{i\varphi_{kx}} \\ \varrho_{ky}e^{i\varphi_{ky}} \end{bmatrix} = \sum_{k=1}^{N} \Psi_k(\boldsymbol{r})e^{i\varphi_k} \begin{bmatrix} \varrho_{kx} \\ \varrho_{ky}e^{i\delta_k} \end{bmatrix}, \tag{2.11}$$

with $\delta_k = \varphi_{ky} - \varphi_{kx}$, $\varphi_k = \varphi_{kx}$ and $\boldsymbol{e}_{k1} = \boldsymbol{e}_x$ and $\boldsymbol{e}_{k2} = \boldsymbol{e}_y$ ($\forall k$), i.e., $\boldsymbol{e}_{k1} \cdot \boldsymbol{e}_{k2} = 0$. The phase δ_k is called *intra*modal phase since it describes the phase difference between the components of one vector mode. This intramodal phase causes the vector mode to be elliptically polarized in general. The phases $\varphi_{kx,y}$ of each mode are measured with respect to a common reference phase whose value is meaningless, since only relative phase differences are of interest. The common reference is chosen to be the phase of the x-component of the fundamental mode. To write eq. (2.11) in a similar way to eq. (2.9) it is necessary to form a unit vector to characterize the polarization of the summarized vector mode:

$$\boldsymbol{U}(\boldsymbol{r}) = \begin{bmatrix} U_1(\boldsymbol{r}) \\ U_2(\boldsymbol{r}) \end{bmatrix} = \sum_{k=1}^{N} \varrho_k e^{i\varphi_k} \Psi_k(\boldsymbol{r}) \begin{bmatrix} a_{kx} \\ a_{ky}e^{i\delta_k} \end{bmatrix} = \sum_{l=1}^{N} c_l \Psi_l(\boldsymbol{r})\boldsymbol{e}_l, \tag{2.12}$$

with $a_{ki} = \varrho_{ki}/\sqrt{\varrho_{kx}^2 + \varrho_{ky}^2}$ and $i = x, y$ and $\varrho_k = \sqrt{\varrho_{kx}^2 + \varrho_{ky}^2}$. The vector $\boldsymbol{e}_l$ now represents the desired unit vector that completely describes the modal polarization state. The amplitudes a_{kx} and a_{ky} as well as the intramodal phase δ_k are sufficient to determine the form and orientation of the modal polarization ellipses.

Note that the expression on the right-hand side of eq. (2.12) is similar to the right-hand side of eq. (2.9) with the difference that the unit vector $\boldsymbol{e}_l$ is now complex to describe the in general elliptical polarization and that the upper limit of the sum is now just the half of the initial limit since every two quasi degenerated linearly polarized modes have been summarized to one vector mode. The term "vector mode" is therfore more specifically used for the composite mode whereas its components are called "linearly polarized modes".

2.5 Correlation Analysis

The expansion in eq. (2.12) is well suited for evaluation with the CGH since the orthogonal components $U_x = |U_x|\,e^{i\varphi_x}$ and $U_y = |U_y|\,e^{i\varphi_y}$ of the vector field $\boldsymbol{U}$ are easily analyzed using a polarizer in front of the hologram. The polarizer is necessary because the CGH can evaluate only scalar fields [35]. The reconstructed fields U_x^{rec} and U_y^{rec}

under orthogonal polarizer orientations read as:

$$U_x^{\text{rec}} = \sum_{l=1}^{N} \varrho_{lx} e^{i\Delta\varphi_{lx}} \Psi_l \quad \text{and} \quad U_y^{\text{rec}} = \sum_{l=1}^{N} \varrho_{ly} e^{i\Delta\varphi_{ly}} \Psi_l, \tag{2.13}$$

where $\Delta\varphi_{lx,y}$ are measured to the respective reference mode of the x,y-component (see fig. 2.7). Note that $U_x^{\text{rec}} = U_x$, but only $|U_y| = \left|U_y^{\text{rec}}\right|$, since the phase difference between the scalar reconstructions $\Delta\varphi_{\text{rel}} = \varphi_y - \varphi_x$, called *relative* phase, is unknown yet and the x-component is chosen to serve as phase reference.

Because the phases $\Delta\varphi_{lx,y}$ refer to the reference mode whose phase is defined as zero for both decompositions, U_y^{rec} has to be multiplied with the intramodal phase term of the reference mode δ_{ref} to obtain the correct phase difference between the vector field components (cf. fig. 2.7):

$$\begin{bmatrix} U_x \\ U_y \end{bmatrix} = \begin{bmatrix} U_x^{\text{rec}} \\ U_y^{\text{rec}} e^{i\delta_{\text{ref}}} \end{bmatrix} = \sum_{l=1}^{N} \Psi_l \begin{bmatrix} \varrho_{lx} e^{i\Delta\varphi_{lx}} \\ \varrho_{ly} e^{i\Delta\varphi_{ly}} e^{i\delta_{\text{ref}}} \end{bmatrix} = \sum_{l=1}^{N} \Psi_l e^{i\Delta\varphi_{lx}} \begin{bmatrix} \varrho_{lx} \\ \varrho_{ly} e^{i\delta_l} \end{bmatrix}, \tag{2.14}$$

where $\delta_l = \Delta\varphi_{ly} + \delta_{\text{ref}} - \Delta\varphi_{lx}$ as can be seen in fig. 2.7. Comparison with eq. (2.11) reveals equality ($\Delta\varphi_{lx} = \varphi_l$), which means that the measurement of the vector field under orthogonal polarizer orientations, in combination with the measurement of the intramodal phase of the reference mode, provides the full information to completely reconstruct the vector field $\boldsymbol{U}$.

Another possibility to correctly reconstruct $\boldsymbol{U}$ from the scalar reconstructions U_x^{rec} and U_y^{rec} is to use the relative phase $\Delta\varphi_{\text{rel}}$ instead of the intramodal phase of the reference mode δ_{ref}:

$$\begin{bmatrix} U_x \\ U_y \end{bmatrix} = \begin{bmatrix} U_x^{\text{rec}} \\ \left|U_y^{\text{rec}}\right| e^{i(\varphi_x + \Delta\varphi_{\text{rel}})} \end{bmatrix}. \tag{2.15}$$
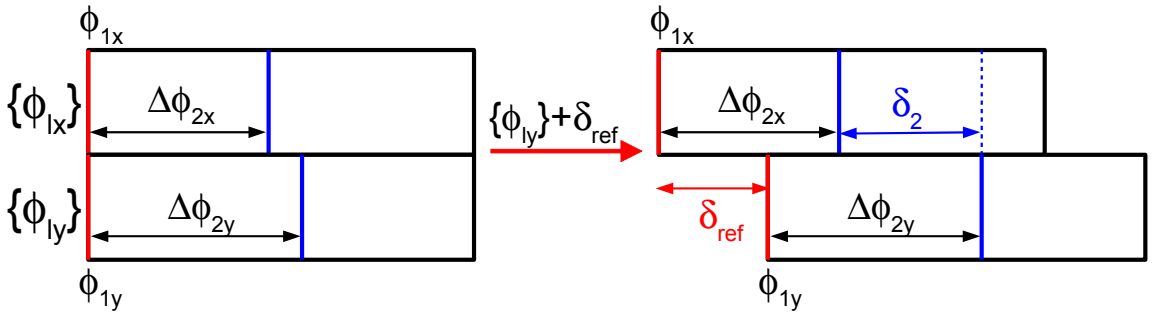

Fig. 2.7 Scheme to visualize the distinction of intermodal and intramodal phase.

The intramodal phases of the modes δ_l, especially that of the reference mode δ_{ref} and the relative phase $\Delta\varphi_{\mathrm{rel}}$, are obtained measuring the Stokes parameters, or in some cases using an alternative approach as described in sec. 2.6. Knowing the components of the vector field, its intensity is given by:

$$I = |U_x|^2 + |U_y|^2, \tag{2.16}$$

where it is worth noticing that δ_{ref} or $\Delta\varphi_{\mathrm{rel}}$ need not to be known for determining the intensity. To calculate the modal spectrum, the intensities at the local optical axes of the diffraction pattern $|W_{lx}|^2$ and $|W_{ly}|^2$ are measured under orthogonal polarizer orientations. Thereby $|W_{lx,y}|^2$ is proportional to $|\langle\Psi_l|U_{x,y}\rangle|^2$ [35]. As a consequence

$$|W_{lx}|^2 + |W_{ly}|^2 \propto |c_l a_{lx}|^2 + |c_l a_{ly} e^{i\delta_l}|^2 = \varrho_l^2(a_{lx}^2 + a_{ly}^2) = \varrho_{lx}^2 + \varrho_{ly}^2 = \varrho_l^2, \tag{2.17}$$

since the amplitudes a_{lx} and a_{ly} are choosen to form a unit vector for each mode (see eq. (2.12) on page 14). Therefore the modal spectrum of the vector field can be easily obtained from the modal spectra measured under orthogonal polarizer orientations, independent of δ_{ref} or $\Delta\varphi_{\mathrm{rel}}$.

2.6 Measurement of the Polarization State

As described in sec. 2.4, the vector field can be decomposed into a set of in general elliptically polarized vector modes leading to an elliptical polarization of the vector field itself. The state of polarization is known if all parameters of the polarization ellipse are known. These parameters determine the form of the ellipse and its orientation with respect to the coordinate axes as well as the sense of rotation the electric field vector will describe in time. There exist two sets of parameters that allow to completely define the ellipse [36]:

- (a_1, a_2, δ) with $a_1, a_2 > 0$, $\delta \in [0, 2\pi]$

- $(a, b, \psi, \mathrm{sgn}\,\chi)$ with $a, b > 0$, $a \geq b$, $\psi \in [0, \pi]$, $\chi \in [-\pi/4, \pi/4]$.

Thereby δ is the phase difference between the x- and the y-component of the field or of the respective vector mode. The remaining quantities are defined in fig. 2.8(a). The parameters of the ellipse can be determined measuring the Stokes parameters or using the alternative approach as detailed in the following sections.
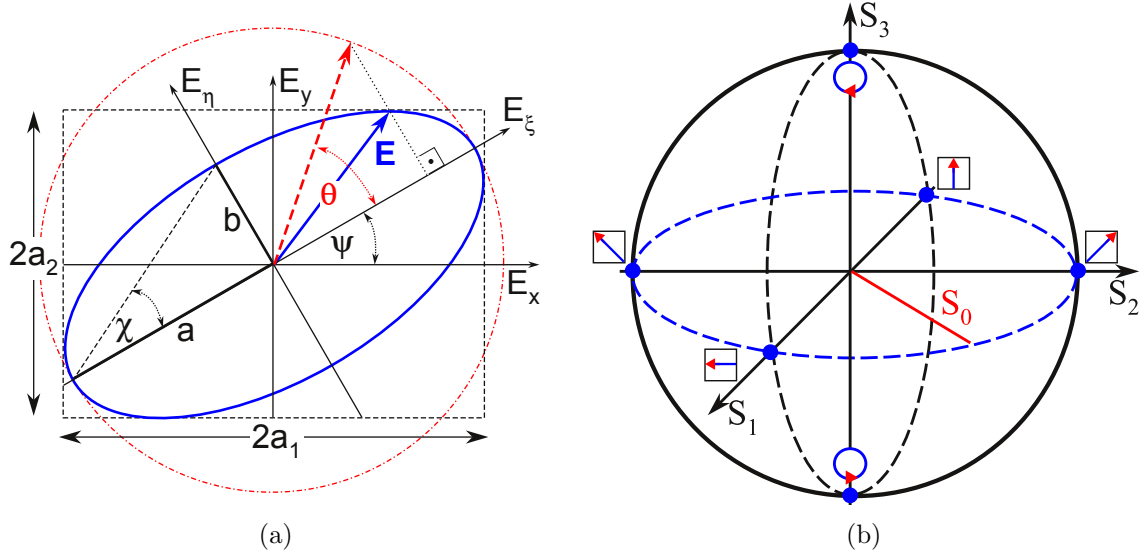
(a)   (b)

Fig. 2.8 (a) Polarization ellipse and definition of corresponding parameters. (b) Definition of the polarization states on the Poincaré sphere.

2.6.1 Stokes Parameters

The Stokes parameters $S_0 \ldots S_3$ can be defined using the parameters of the polarization ellipse of the first or second set [36]:

$$
\begin{aligned}
S_0 &= a_1^2 + a_2^2 & S_0 &= a^2 + b^2 \\
S_1 &= a_1^2 - a_2^2 & S_1 &= S_0 \cos 2\chi \cos 2\psi \\
S_2 &= 2a_1 a_2 \cos \delta & S_2 &= S_0 \cos 2\chi \sin 2\psi \\
S_3 &= 2a_1 a_2 \sin \delta & S_3 &= S_0 \sin 2\chi
\end{aligned}
\tag{2.18}
$$

The Stokes parameters can be understood as spherical coordinates leading to the Poincaré sphere with radius S_0 (cf. fig. 2.8(b)). The poles of the sphere ($S_3 = \pm S_0$) represent circular polarization, whereas the equator ($S_3 = 0$, blue dashed line) marks linear polarization. All other points correspond to elliptical polarization. The sense of rotation and the orientation of the polarization ellipses are defined in fig. 2.8(b). Measuring the Stokes parameters allows the calculation of all parameters of the polarization ellipse. It is important to note that the CGH-based measurement technique equally allows to determine the Stokes parameters spatially ($a_{1,2} = |U_{x,y}|$, $\delta = \Delta\varphi_{\mathrm{rel}}$) and modally ($a_{1,2} = \varrho_{lx,y}$, $\delta = \delta_l$) resolved.

To determine the Stokes parameters, seven measurements are necessary [14]. First the intensity of the vector beam is measured behind a polarizer with angular orientations of 0°, 90°, 45° and 135° with respect to one of the coordinate axes, leading to the

parameters S_1 and S_2. Second the intensity is measured behind the pair of a quarter-wave plate and a polarizer, whereas the former should be oriented with an angle of $0°$ and the polarizer with an angle of $45°$ and $135°$ to the chosen coordinate axes, which leads to the parameter S_3. Finally the intensity of the vector beam is measured without any additional optical components leading to the parameter S_0. The Stokes parameters form the Stokes vector:

$$\boldsymbol{S} = \begin{bmatrix} S_0 \\ S_1 \\ S_2 \\ S_3 \end{bmatrix} = \begin{bmatrix} I \\ I_{0°} - I_{90°} \\ I_{45°} - I_{135°} \\ I_{rc} - I_{lc} \end{bmatrix}, \tag{2.19}$$

where $I_{0°}$, $I_{90°}$, $I_{45°}$ and $I_{135°}$ are the intensities behind the polarizer, I_{rc} and I_{lc} are the intensities behind the pair of quarter-wave plate and polarizer, and I is the unfiltered intensity. In the case of completely polarized light, $S_0 = \sqrt{S_1^2 + S_2^2 + S_3^2}$ holds, so that the full description of the polarization state of the vector beam requires only six measurements. Note that the mentioned intensities can be represented by the reconstructed or measured intensities as well as by the modal powers.

2.6.2 Alternative Approach

Another way to identify the polarization state, either of the entire vector beam or of each mode seperately, is to analyze the beam after a single polarizer that is rotated from $0°$ to $360°$ in a small step size (e.g., $10°$). For elliptical polarization in front of the polarizer, the intensity behind is expected to vary as $C_1 \sin^2(\alpha + \alpha_0) + C_2$, where α is the orientation angle of the polarizer and C_1, C_2 and α_0 are constants determined by a fit (C_2 is zero for linear polarization). With these values there is easy access to the main axes of the polarization ellipse a, b and the orientation angle ψ:

$$\begin{aligned} a &= C_1 + C_2 \\ b &= C_2 \\ \psi &= (k+1)\frac{\pi}{2} - \alpha_0, \end{aligned} \tag{2.20}$$

where k is chosen such that $\psi \in [0, \pi]$. The drawback of this method is, that it does not provide any information about the sense of rotation of the electric field vector, i.e., the sign of χ remains unclear. Hence, the Stokes parameters are known, except for the sign of S_3. Another disadvantage is the greater measurement effort compared to the measurement of the Stokes parameters, that could be eliminated by using a stepping motor for the rotation of the polarizer. The advantage is, that the parameters a, b and

Ψ are measured directly, and are not a solution of a equation system as in the case of the Stokes parameters. If there is one linearly polarized vector mode contained in the mode mixture, all other intramodal phases are known and the field reconstruction is possible.

The measurement of the Stokes parameters will be the preferred method for measuring the polarization state in this work, since it provides the full information with less measurement effort.

Chapter Summary

The modes of the investigated MCF are calculated using a scalar CMT and several vectorial mode solvers. Concerning the field patterns and the effective indices of the modes, the comparison with a commercial FEM solver reveals highest accuracy for the multipole method. The results of the CMT become inaccurate for increasing wavelength but are in good agreement with the FEM solver at 633 nm. The modes are approximately described using the effective index theory.

Stronger coupling between individual cores leads to a growing synchronization of phases and reduces the number of modes. The modes are nearly transverse with a dominating transverse component. This property is used to summarize two degenerated linearly polarized modes to one vector mode. The composite vector modes build a complete orthogonal set allowing to expand arbitrary vector fields.

The reconstruction of a vector field is described by modal decomposition of its scalar components, where the correct phase relation is determined from the measurement of the Stokes parameters.

3 Experiments

3.1 Measurement Setup

The experimental setup as shown in fig. 3.1 basically consists of the laser source with corresponding beam preparing components (blue), the MCF as object of investigation (green), and the analyzing system (red).

For this work, three lasers are electively used as light source: a helium neon laser ($\lambda = 633\,\text{nm}$), a laser diode ($\lambda = 780\,\text{nm}$) and a Nd:YAG laser ($\lambda = 1064\,\text{nm}$). A phase plate and a half-wave plate, respectively, are optionally used to alter the shape and the polarization of the input beam. The beam is focussed onto the fiber end facet with a microscope objective (MO, $f = 10\ldots25.4\,\text{mm}$), where the distance of the laser and the focal length of the MO are adjusted to attain the optimal beam radius. Thereby, the beam radius on the end facet of the fiber should match the mode field radius that is $10\,\mu\text{m}\ldots13\,\mu\text{m}$ ($\lambda = 633\,\text{nm}\ldots1064\,\text{nm}$) for the examined fiber. The laser beam parameters are determined by performing an ISO-conform caustic measurement. To couple light into the fiber, a manual three-axes coupling stage and a six-axes nano-positioning stage with minimal movement range of $1\,\mu\text{m}$ and $100\,\text{nm}$, respectively, and $2\,\mu\text{rad}$ are used. A manual three-axes stage is used to couple the light out. Thereby the fiber end facet can be rotated to ensure correct orientation of the mode fields with
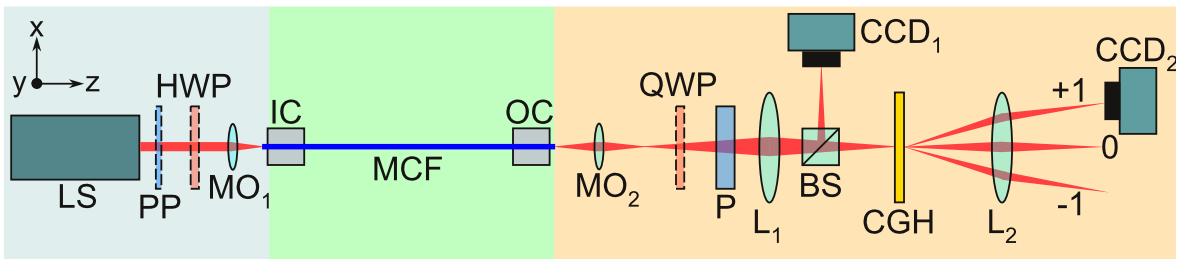

Fig. 3.1 Topview of the measurement setup: blue: laser source and beam preparation, green: object of investigation, red: analysis system. LS laser source, PP phase plate (optional), HWP half-wave plate (optional), $\text{MO}_{1,2}$ microscope objectives, IC input coupler, MCF multi-core fiber, OC output coupler, QWP quarter-wave plate (optional), P polarizer, $\text{L}_{1,2}$ lenses, BS beam splitter, $\text{CCD}_{1,2}$ CCD cameras, CGH computer-generated hologram.

respect to the hologram. The magnification of the near field results from the ratio $f(L_1)/f(MO_2)$. Used magnifications are 37.5, 45 and 62.5.

After passing through a quarter-wave plate and a polarizer, that are necessary for the determination of the polarization state, the beam is split in two branches. Via the beam splitter, the fiber end facet is simultaneously imaged onto the CGH and a CCD camera for recording the near-field intensity (CCD_1). The CGH diffracts the beam in various orders. The pattern of the first diffraction order is imaged onto a second CCD camera (CCD_2), whose image is used to determine the modal spectrum of the beam for the scalar projection provided by the polarizer. Thereby the focal length of lens L_2 is chosen to be $18\,mm$ to match the size of the diffraction pattern with the one of the CCD chip (maximum resolution: $4.4\,\mu m$ (1600×1200 pixels) and 16 Bit).

3.2 Computer-generated Hologram

The used computer-generated holograms are binary amplitude holograms with a Lee-type coding [37]. A hologram consists of 512×512 Lee-cells. Each cell with dimension $16 \times 16\,\mu m^2$ is composed of four subcells with dimension $4 \times 16\,\mu m^2$, that encode positive and negative real and imaginary parts of one complex number of the transmission function of the hologram. The calculation of the transmission function to design the first diffraction order in the far field is particularized in [35].

The hologram is written by laser lithography in a $70\,nm$-thick layer of chromium, deposited on a glass substrate. The smallest structure size that can be written is $700\,nm$. The quality of the manufactured holograms is checked by illumination with a plane wave with approximately constant amplitude over the aperture of the hologram. A plane wave of constant amplitude multiplied with the transmission function of the hologram yields the far field patterns of the modes at the local optical axes in the Fourier plane of the hologram [35]. This is examined for the used holograms by comparison with the simulated diffraction patterns, revealing very good agreement and thus indicating a high quality of the fabricated holograms.

3.3 Detection of Higher Order Modes

The calculation of the modes of the MCF is based on an idealized index distribution with rectangular index steps, which defines the number and the shape of modes. However, the true index distribution is not exactly known. It is most likely that the cores have a rather gaussian-shaped index profile than a rectangular one, which reduces the

number of propagating modes as well as inevitable bending of the fiber does. There-
fore it is interesting to investigate how many modes can actually be attested. This is
achieved by searching for mode mixtures with high portion ($> 60\%$) of a distinct higher
order mode (HOM). Using a phase plate in front of the input coupler and transversally
displace the fiber with respect to the microscope objective, the overlap to HOMs was
enhanced. For this experiment a straight and short ($\approx 40\,\text{cm}$) fiber was used to retain
the excited HOMs. Fig. 3.2 depicts mode mixtures that contain the highest measurable
modes at 1064 nm, 780 nm and 633 nm to a large fraction.

At 1064 nm the fiber is single-mode, in contrast to the simulations that predict three
propagating modes. The residual fractions of mode 2 and 3, as seen in fig. 3.2, are
caused by the CCD background (cf. sec. 3.9), and by deformation of the near field
and the emerging beam induced by microbending (cf. sec. 3.5.1) and by aberrations of
external optical components such as lenses and beam splitter.

The highest order mode with high power fraction at 780 nm is mode 5, whose appear-
ance is clearly visible in the measured near field intensity. However, also mode 6 could
be measured up to a power fraction of 16 % in other mixtures.

At 633 nm, simulations predict twelve modes. The highest order mode that could be
attested at this wavelength is mode 7 (fig. 3.2, right). The existance of the modes 8 to
12 is therefore unlikely. But it is possible that a coupling situation adapted to distinct
HOMs in combination with a further reduced fiber length could reveal the propagation
of those modes, especially that of mode 8, since its propagation constant is very close
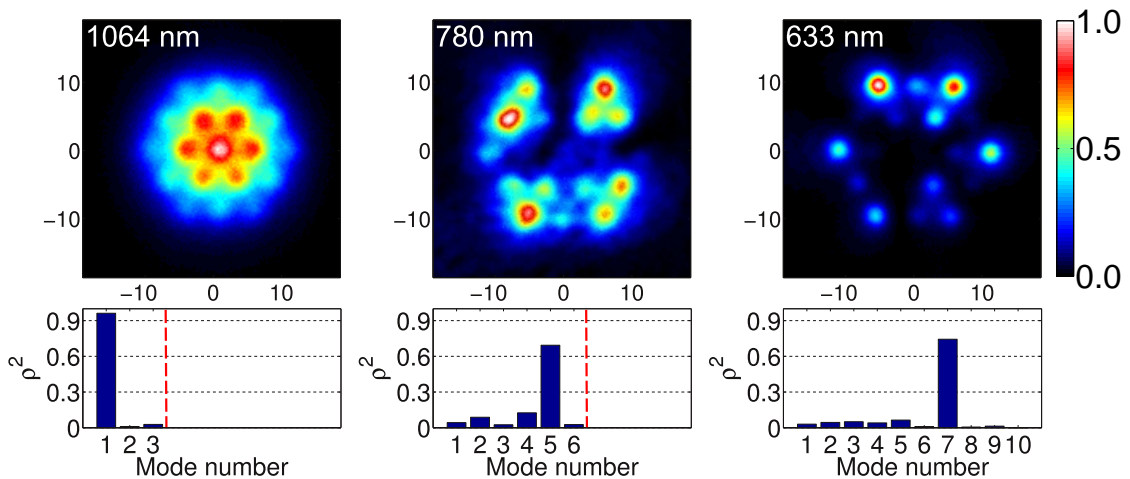to the one of mode 7.

Fig. 3.2 Highest detectable modes at 1064 nm (left, 96 % Mode 1), 780 nm (middle, 69 %
Mode 5) and 633 nm (right, 74 % Mode 7). Upper row: measured normalized near
field intensities (coordinates in µm). Lower row: corresponding modal spectra.
The red dashed line marks the modal cut-off.

3.4 Complete Field Reconstruction

Analyzing a vector beam with a polarizer in front of the hologram enables the reconstruction of the vector field intensity with its corresponding modal spectrum as described in sec. 2.5. Combining the CGH-technique with the measurement of the Stokes vector, the correct phase relation between the reconstructed vector field components can be determined. With this, the vector field is completely described, based on the well-known fields of the modes.

To determine the Stokes parameters it is necessary to measure the beam intensity after a pair of a polarizer and a quarter-wave plate, as described in sec. 2.6.1. These intensities with corresponding modal spectra are depicted in fig. 3.3 for a selected sample beam. The variation of the relative modal weights, of the shape of the intensity pattern, and of the power implies, that the polarization is spatially varying and that different vector modes have quite different polarization states. The measurement of the six intensity distributions as shown in fig. 3.3 enables the calculation of the vector beam intensity, the overall modal spectrum and the local and modal polarization.
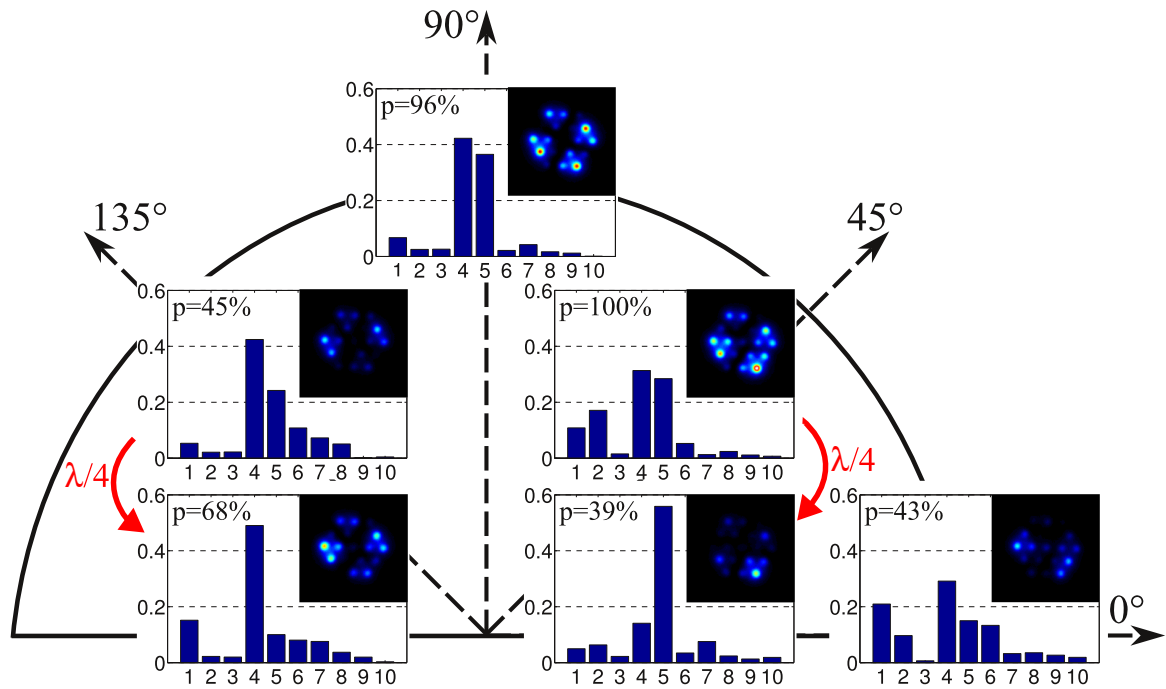
Fig. 3.3 Measured intensities and modal spectra behind a polarizer and a pair of polarizer and quarter-wave plate, respectively. The polarizer orientation is denoted with 0°, 45°, 90° and 135°. The red arrows mark the measurement at the same polarizer orientation, but with quarter-wave plate in the optical path. The power, referred to the one at 45°, is denoted by p.

3.4.1 Intensity and Modal Spectrum

To obtain the vector beam intensity and its modal spectrum, two intensity measurements under orthogonal polarizer orientations are necessary. Thereby the two intensity distributions are simply added up[1] as described by eq. (2.16) on page 16. The power of the reconstructed intensities is given by the power of the measured near field intensities, obtained by integration. The modal spectrum is calculated analogously via eq. (2.17) on page 16.

The results, obtained for the sample beam of fig. 3.3, are depicted in fig. 3.4. As can be seen, mode 4 and 5 dominate the beam with $68\,\%$ of the power leading to a near field intensity with four lobes rotated $\approx 20°$ with respect to the coordinate system. The remaining vector modes, that have a power fraction of $32\,\%$, increase the intensity in the nodal lines, which becomes clear if compared to the clear dark nodal lines in the scalar measurement at $90°$ in fig. 3.3 ($80\,\%$ of the power in mode 4 and 5). The comparison between measured and reconstructed intensity is done using a two-dimensional cross-correlation coefficient as defined in [35], that is $91\,\%$ in this case. Considering that 28 measured values with some uncertainty contribute to the reconstruction, the accordance between both intensity distributions is very good.
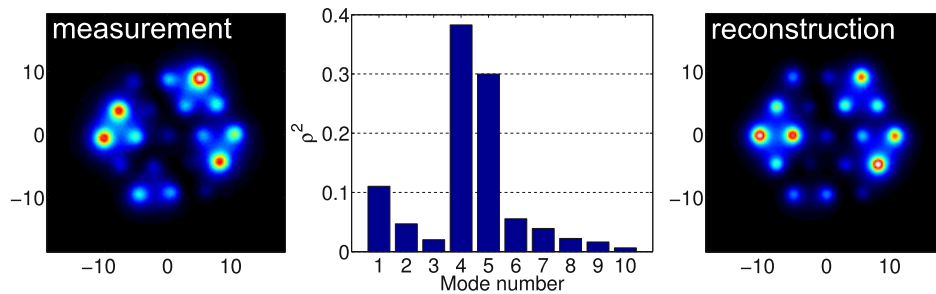

Fig. 3.4 Measured and reconstructed intensity (in each case normalized to maximum value) with corresponding modal spectrum of the beam analyzed in fig. 3.3. The cross-correlation coefficient comparing both intensity patterns amounts to $91\,\%$. Axes dimensions in µm.

3.4.2 Local Polarization and Local Phase

To determine the polarization state for each point of the field, the Stokes parameters have to be calculated using eq. (2.19) on page 18, as depicted in fig. 3.5 for the sample beam of fig. 3.3. Thereby fig. 3.5 compares the Stokes parameters calculated from the

---

[1]The vector beam intensity could be measured directly by recording with a CCD camera without the polarization manipulating elements. Instead, the two scalar near field intensities are added up to keep the CGH adjusted.
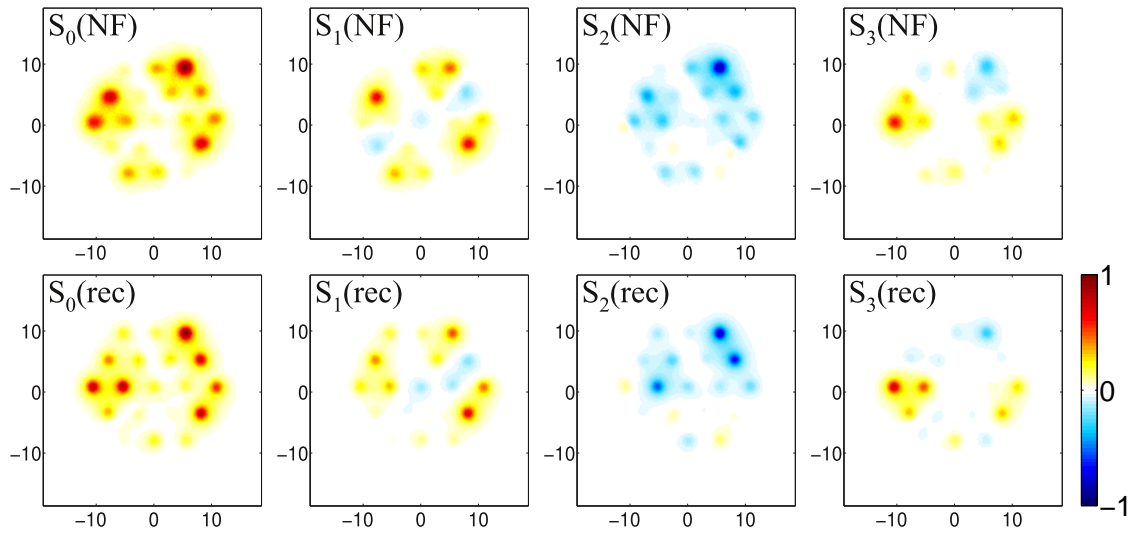
Fig. 3.5 Stokes parameters calculated from the measured intensities with normalization to the maximum value of $S_0(\mathrm{NF})$ (upper row) and from the reconstructed intensities with normalization to the maximum value of $S_0(\mathrm{rec})$ (lower row). Axes in µm.

measured and reconstructed intensity distributions.

Deviations mainly occur due to the discrepancies between the scalar, measured and reconstructed intensities, that are caused by the uncertainties of the modal amplitudes and phases (see sec. 3.9). Regarding the near field measurements, a crucial point is the transversal realignment of the intensity patterns since a rotation of the polarizer shifts the beam on the CCD chip. Especially, the computation of the parameters $S_0 \ldots S_3$ would yield incorrect results if the shift would not be corrected[2]. In the case of the MCF the realignment is done easily since the individual cores are visible in the near field intensity pattern.

Using eq. (2.18) on page 17, the phase difference between two scalar orthogonal reconstructions, and the intramodal phase of the reference mode can be calculated. With this, the field is characterized completely allowing the determination of local polarization ellipses. In addition, the knowledge about the phase relation of the vector field components allows the derivation of a new quantity, the so-called *local* phase θ as defined in fig. 2.8 on page 17.

Consider the electric field vectors rotating with time at each point of the field in a clockwise or counter-clockwise sense along their local polarization ellipses. At a fixed time, each field vector will point in a different direction. The angle to the major axis is defined to be the local phase.

Fig. 3.6 depicts the sample beam intensity with local polarization ellipses drawn at

---

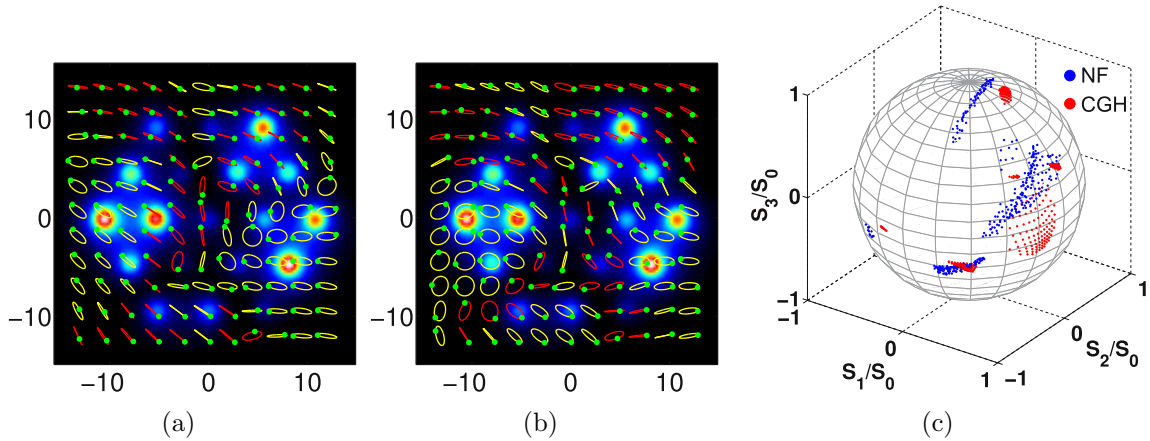[2]The high spatial frequencies in the pattern of the near field cause a high sensitivity to transverse shift.

Fig. 3.6 Local polarization of the sample beam, calculated using the intramodal phase of the reference mode (a) and using the relative phase (b). Axes in µm. The color of the ellipses marks the sense of rotation: right-handed (yellow), left-handed (red). The green points mark the starting point of the electric field vector at a fixed time - the local phase. (c) Stokes parameters of the vector field (points with intensity of at least 40 % of the maximum intensity) presented on the Poincaré sphere.

discrete points, where the color of the ellipses marks the sense of rotation, and the green points denote the starting points of the electric field vectors at a fixed time $t = 0$. Fig. 3.6(a) and fig. 3.6(b) compare the two possibilities to reconstruct the phase of the y-component of the vector field (eq. (2.14) and (2.15) on page 15). The comparison reveals agreement in principle, but at a closer look there are some discrepancies regarding the shape of the ellipse, the sense of rotation and the local phase. This is explained by the uncertainty of the phase distributions of the field components[3] as well as that of the relative and intramodal phase, which results from the uncertainty of the Stokes parameters (see above).

In fig. 3.6(c) the local polarization is presented on the Poincaré sphere. Despite the loss of spatial information, four main polarization areas are visible. The results obtained from the direct near field measurement, and from the reconstruction using the CGH agree in general. Deviations occur due to the mentioned shift affecting the near field measurement, and a cross-correlation coefficient smaller than one. The spatially varying polarization, as for the sample beam of fig. 3.6, is a feature of beams consisting of multiple modes. This is confirmed regarding fig. 3.7, where the local polarization is investigated for a excitation wavelength of 1064 nm. At this wavelength the MCF is single-mode leading to global polarization, i.e., all polarization ellipses have the same

---

[3]At 633 nm the phase distribution of a field component is composed of the phases of ten modes, each intermodal phase resulting from four intensity measurements.
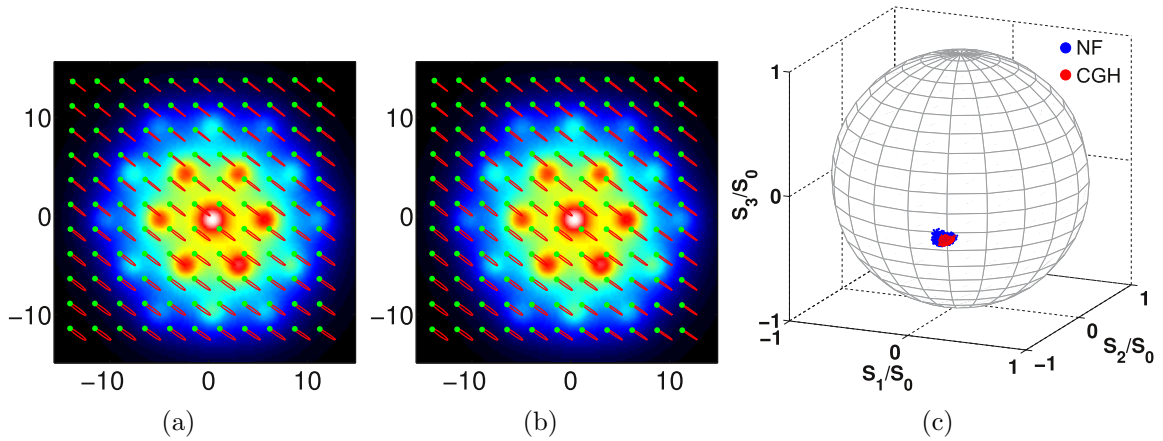
Fig. 3.7 Local polarization of a beam at 1064 nm. Polarization ellipses and local phase using (a) the intramodal phase of the reference mode and (b) the relative phase (axes dimensions in µm). Colors and labeling as in fig. 3.6. (c) Stokes parameters of the vector field (points with intensity of at least 40 % of the maximum intensity) presented on the Poincaré sphere.

shape and point in the same direction. In addition, the local phase is flat meaning that all points in the field are in-phase. The Poincaré representation exhibits very small spreading of the local polarization states and the results obtained from near field measurement and CGH-reconstruction are in excellent agreement (fig. 3.7(c)). Further, the reconstructions of the polarization ellipses, using the intramodal phase (fig. 3.7(a)) and the relative phase (fig. 3.7(b)), respectively, yield same results at 1064 nm. This illustrates the influence of the number of modes on the accuracy of the analysis procedure.

3.4.3 Modal Polarization

In sec. 3.4.2 the Stokes parameters of the vector field are used to reconstruct the local polarization and the local phase. Beyond that, the CGH allows to determine modal Stokes parameters using the absolute modal spectra. The modal polarization for the sample beam of fig. 3.6 is depicted in fig. 3.8 in form of points on the Poincaré sphere and normalized polarization ellipses. It can be seen that the modal polarization is quite diverse, but S_2 is mainly negative and S_3 mainly positive, which means that the polarization ellipses are mainly oriented $90° \ldots 180°$ to the x-axis and the sense of rotation is dominantly right-handed.
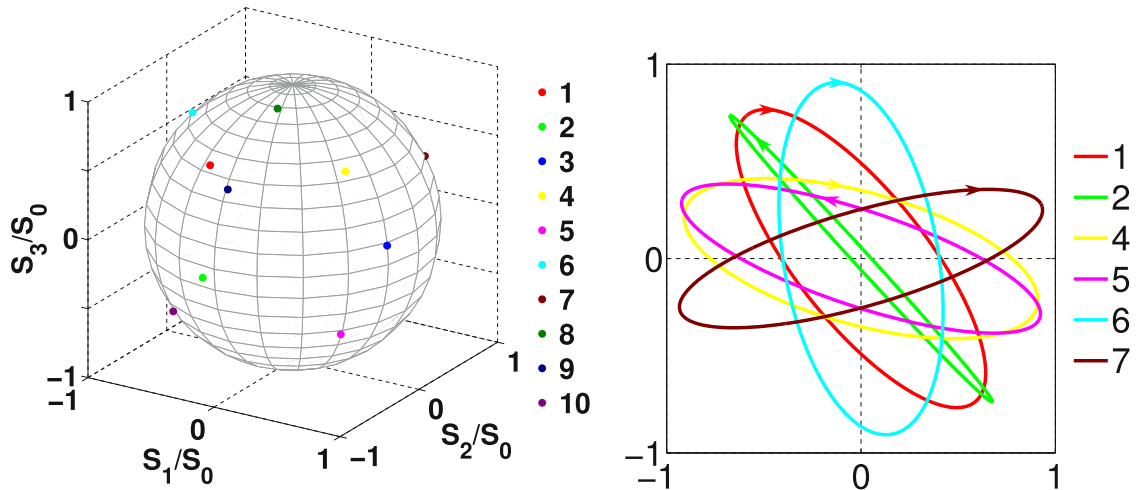
Fig. 3.8 Modal polarization of the sample beam depicted as points on the Poincaré sphere (left) and as normalized polarization ellipses of modes with power fraction larger than 3 % (right, axes in a.u.).

3.4.4 Comparison of Polarization Measurement Techniques

Sec. 2.6 outlines two polarization measurement techniques. To compare both methods, a mode mixture at 780 nm is chosen and the modal polarization ellipses are calculated. Fig. 3.9 depicts the modal ellipses for all six modes, calculated from the measurement of the Stokes parameters and from the 360°-rotation of the polarizer. Whereas the orientation angle is in excellent agreement (maximum deviation of 4°), the absolute value of the ellipticity $|\varepsilon| = |\sin\chi|$ partially differs (maximum deviation 0.65).
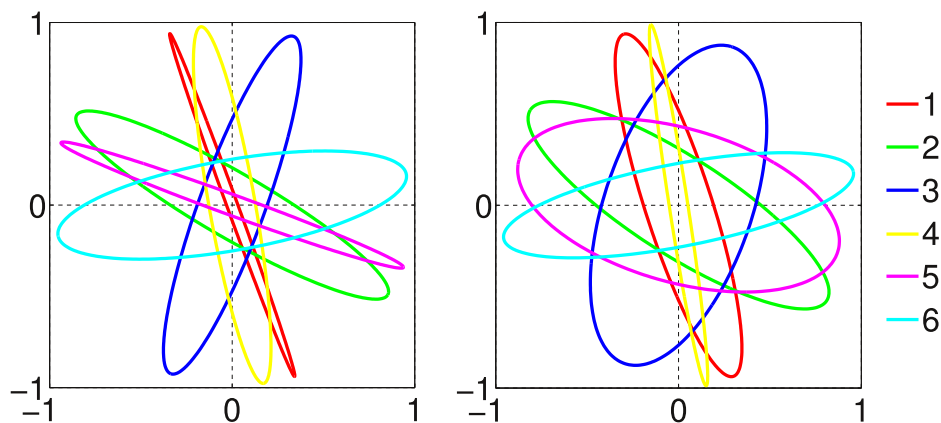

Fig. 3.9 Normalized modal polarization ellipses of a beam at 780 nm, calculated from a full rotation of a polarizer (left), and from the Stokes parameters (right), respectively. Axes in a.u. Relative modal content of mode 1...6 in %: 13.5, 36.4, 10.2, 8.1, 26.7 and 5.0.

The discrepancies are refered to the uncertainties of the modal Stokes parameters as well as to the deviations of the modal power curves from the $\sin^2$-fits in the case of the full rotation of the polarizer (cf. sec. 3.9).

3.5 Modal Content and Polarization

In sec. 3.4 the complete reconstruction of the vector field is demonstrated including the modal spectrum and the vector beam intensity as well as the local polarization, the local phase and the modal polarization. Now, the ability of measuring those quantities is used to get a deeper insight into the modal properties of the MCF by investigating the behavior by systematic variation of parameters such as bending diameter, vertical pressure, input polarization, or fiber length.

3.5.1 Dependence on Bending Diameter

Bending a fiber induces several effects that affect the fiber geometry and its index distribution. First, it occurs a path length difference or phase retardation between inner and outer side of the bent fiber, i.e., the side of the fiber facing the bending center and the opposite. This effect can be numerically described by an equivalent straight fiber with altered index distribution $n'(x, y)$ where the phase retardation of the outer side is attributed by an increased refractive index [38]:

$$n'(x, y) = n(x, y) \, e^{2x/D_{\mathrm{B}}} \tag{3.1}$$

for bending the fiber in the xz-plane and with $n(x, y)$ the index distribution of the unperturbed fiber and D_{B} the bending diameter.

Second, the bend leads to tension at the outer side and compression at the inner side. The photoelastic effect therefore causes the index to increase slightly at the compressed side. This counteracts the previously described phase retardation which is considered by using an effective bending diameter $D_{\mathrm{B}}^{\mathrm{eff}} \approx 1.28 \, D_{\mathrm{B}}$, where the number is specific for silica [38].

Since bending changes the refractive index along a certain direction it induces a birefringence, i.e., the x- and y-component of each vector mode generally propagate with different phase velocities or, in the theory of this work, the intramodal phase becomes unequal zero. This is in contrast to the straight fiber, in which both components propagate with approximately the same velocity (difference of the effective indices in the order of 10^{-8}), since the fiber is weakly guiding.

The equivalent index distribution for a bending diameter of 10 cm is simulated in fig. 3.10(a) as a profile along the x-direction in comparison with the corresponding profile of the straight fiber. Additionally, the two dashed lines mark the effective index of the fundamental mode at 633 nm (red) and 1064 nm (black). Defining a critical bending diameter $D_{\mathrm{B}}^{\mathrm{crit}}$ as the diameter where the effective indices of the modes fall below the maximal cladding index at the edge of the computational domain ($48 \times 48\,\mu\mathrm{m}^2$), $D_{\mathrm{B}}^{\mathrm{crit}}$ is 14 cm, 57 cm and 56 cm for the modes at 1064 nm, and 6.6 cm, 9.2 cm, 9.8 cm, 13.2 cm, 14.2 cm, 16.2 cm, 23 cm, 29 cm, 45 cm, 46 cm, 158 cm and 167 cm for the modes at 633 nm. Regarding $D_{\mathrm{B}}^{\mathrm{crit}}$, the large difference between the two HOMs and the fundamental mode at 1064 nm and of mode 11 and 12 to the lower order modes at 633 nm indicate, that these modes are very sensitive to pertubations and might not be propagating in real experimental environments, concerning for example microbends (cf. below and sec. 3.3).

The bending induced change of the refractive index leads to a mode field distortion at the place of bending [39]. This behavior can be observed at 1064 nm by applying local pressure, e.g., caused by the fiber clamps as seen in fig. 3.10(b), where the short bend length leads to no significant power loss. Note that at this wavelength there are no HOMs that could explain the shift of the barycenter of the intensity. The measured distortion of the near field intensity is compared to a simulation at a bending diameter of 21.1 cm. This number is found by an optimization based on the cross-correlation coefficient.
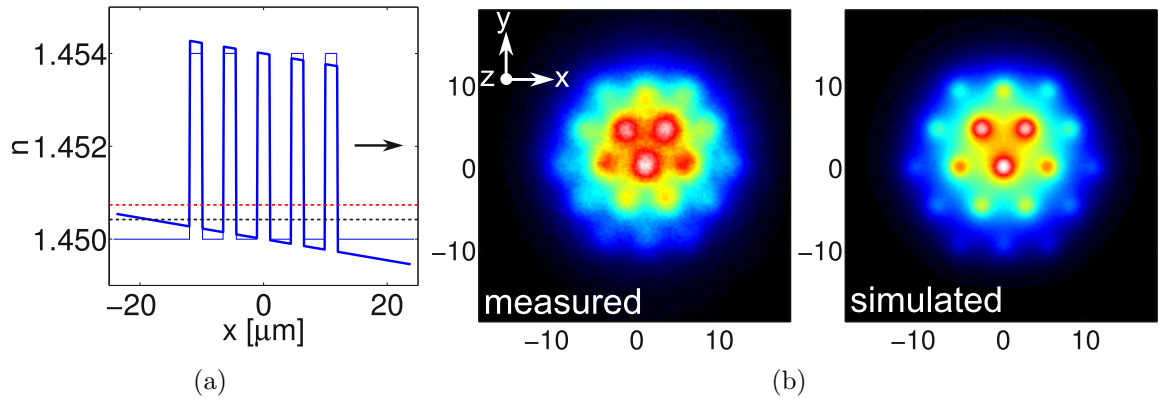

(a)   (b)

Fig. 3.10 (a) Bending induced deformation of the index distribution (intense blue line) for a bending diameter of 10 cm and bendig in the xz-plane. Additionally, the unperturbed core and cladding index (faint blue line) and the effective indices of the fundamental mode at 633 nm (dashed red line) and 1064 nm (dashed black line) are shown. The arrow points towards the center of the bend. (b) Bending induced distortion (bending in yz-plane). Left: measured near field intensity at 1064 nm. Right: simulated intensity for $D_{\mathrm{B}} = 21.1$ cm.

The good correlation of both intensity distributions of 98 % and the disappearance of the distortion by holding the fiber only with adhesive strips indicate, that the observed effect is explained by microbending and not by aberrations, caused by lenses or the beam splitter, or by an inclined fiber cleave.

To exemplarily demonstrate the detection of modal effects at bending, a mode mixture with an initially high content of HOMs (99 %) is excited. Fig. 3.11 depicts the relative modal spectrum when bending the fiber in a half circle with diameters ranging from 30 cm to 7 cm. Thereby, only the first ten modes are analyzed which is justified by the weak guidance of mode 11 and 12 and their neglectable excitation efficiencies. While bending the fiber the light injection remains unaltered.

The modal spectra reveal that the relative content of the fundamental mode increases from initially 1 % to 62 % while the total power decreases from 77 µW to 3 µW, which constitutes a power loss of 14 dB at 7 cm. This behavior is well known [40], and can be applied to enhance the beam quality with the drawback of power loss. On the contrary, the relative and absolute power of mode 4 and 5 continuously drops with increased bending, as seen in fig. 3.11.

Additionally, the behavior of the relative and absolute modal power in fig. 3.11 points to power transfer processes, which are most presumable for modes with close effective indices, such as mode 2 and 3 (cf. tab.2.1 on page 9). The oscillating power curves of mode 2 and 3 (inset of fig. 3.11) indicate a power exchange of both modes in the range of $D_B = 14 \ldots 9$ cm.
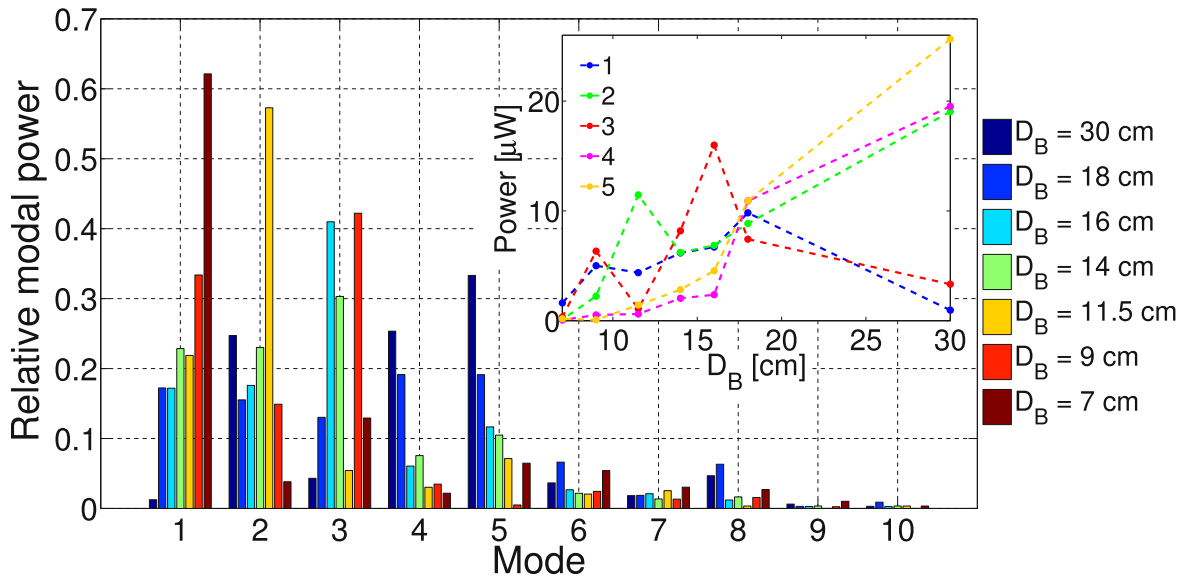

Fig. 3.11 Modal spectrum as a function of the bending diameter D_B. The inset shows the absolute modal power for the first five modes (dashed lines to guide the eye).

Further, the power grow of mode 3 at bending diameters from $18\ldots16\,$cm can not be solely explained by power transfer from mode 2, because the power drop of mode 2 is distinctly less than the strengthening of mode 3. Therefore, also power flow from the fundamental mode or the modes 4 and 5 are reasonable. Below $9\,$cm, all modes suffer from power loss due to radiation. Thereby, the power of mode 2 drops faster than that of mode 3, which can be explained by the larger extension of mode 2 in bending direction. The marginal power fractions of mode 9 and 10 affirm that mode 11 and 12 need not to be considered in the modal expansion.

The dependence of the modal polarization state on the bending diameter is depicted in fig. 3.12 regarding the orientation angle Ψ of the polarization ellipses, the normalized difference of the modal amplitudes in x- and y-direction $(a_1 - a_2)/(a_1 + a_2)$ with $a_{1,2} = \varrho_{x,y}$, and the intramodal phase δ (uncertainty considerations cf. sec. 3.9). The excitation light from the helium neon laser is linearly polarized (polarization extinction ratio PER $= 34\,$dB) in y-direction as marked with solid black lines in fig. 3.12. It can be seen that except for the fundamental mode that preserves the polarization direction of the input light, all modes experience strong rotations of the polarization ellipses with bending. Effects that cause such rotations are, e.g., twist-induced optical activity [41], a change of the intramodal phase caused by an altered birefringence, polarization dependent loss or power coupling. Induced optical activity can be excluded, because the fiber was not twisted on purpose and the proportionality factor between twist angle and polarization rotation angle is far too small to explain the large measured rotations [41]. Since the fiber is weakly guiding, a polarization dependence of the bending loss is neglectable [42]. In fact, power coupling between the two degenerated linearly polarized modes and a changing intramodal phase explain the polarization rotation (cf. 3.12 middle and right). This behavior is expected, since the cross section of the investigated MCF does not include polarization-maintaining elements.
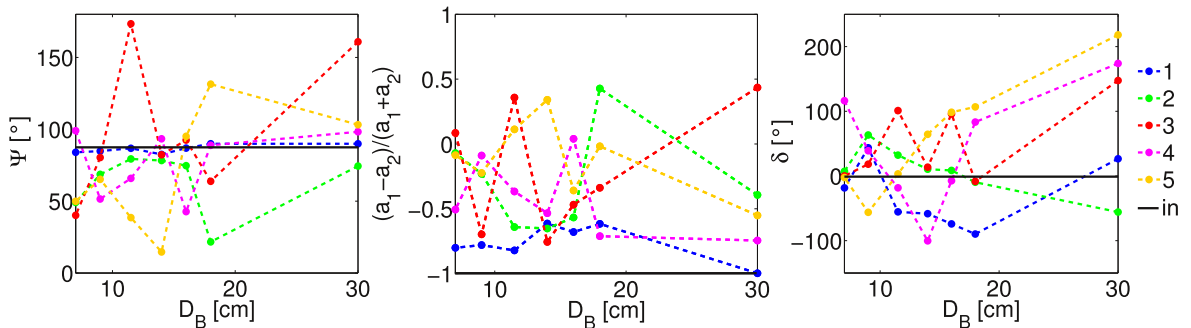

Fig. 3.12 Modal polarization for the first five modes as a function of the bending diameter D_B in comparison with the polarization of the input light: orientation angle (left), normalized difference of modal amplitudes (middle) and intramodal phase (right).

Therefore, the propagation constants of each two polarization-degenerated modes are very close favoring power coupling and yielding a high sensitivity to statistical birefringence [43].

The bending behavior of the MCF at 1064 nm is illustrated in fig. 3.13. The exciting Nd:YAG laser is linearly polarized in x-direction (PER = 15.4 dB) and its polarization is rotated $\approx 136°$ using a half-wave plate to excite both polarization components of the fundamental mode. Evidently, the polarization of the fundamental mode is stable down to a bending diameter of 19 cm and agrees in orientation with the input light. Stronger bending increases the intramodal phase and some power couples into the x-component leading to a rotation of the polarization ellipse. The power loss at 16.5 cm amounts to 16.2 dB, which demonstrates the weaker guidance at 1064 nm, compared to 633 nm.
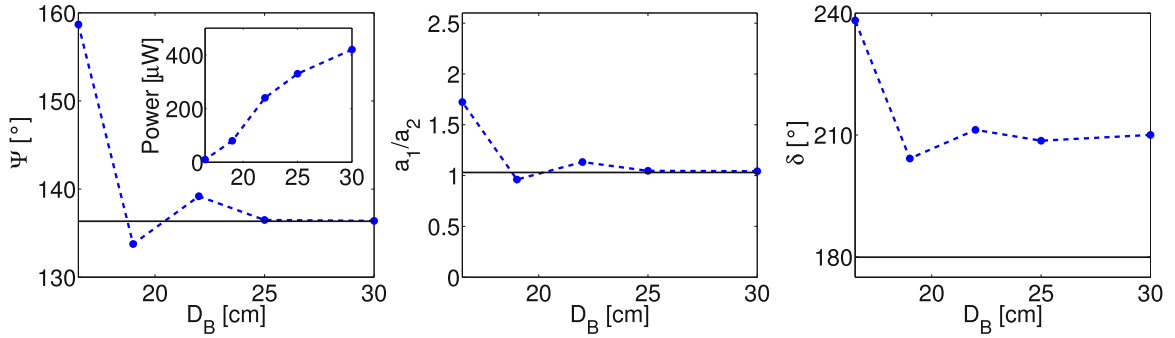

Fig. 3.13 Polarization of the fundamental mode (dashed lines) at 1064 nm as a function of the bending diameter D_B in comparison with the polarization of the input light (solid line): orientation angle (left), ratio of modal amplitudes (middle) and intramodal phase (right). The inset depicts the total power.

3.5.2 Dependence on Vertical Pressure

To investigate the reaction of the modes on vertical pressure (in direction of -y) the fiber is jammed between two parallel plates that are compressed via a screw clamp. Therewith, the fiber is uniformly strained along 2 cm. A laser diode (780 nm, PER = 22 dB) provides the excitation light and is rotated to enable a polarization with major axis oriented at $\approx 135°$. While straining the fiber the light injection is unaltered.

The two major effects that are to be expected to change the modal properties are strain-induced birefringence due to the photoelastic effect, and deformation of the fiber geometry leading to geometrical birefringence [44].

Fig. 3.14 depicts the behavior of the modal power and polarization as a function of the rotation angle of the screw. Thereby the acting vertical force can be assumed to scale
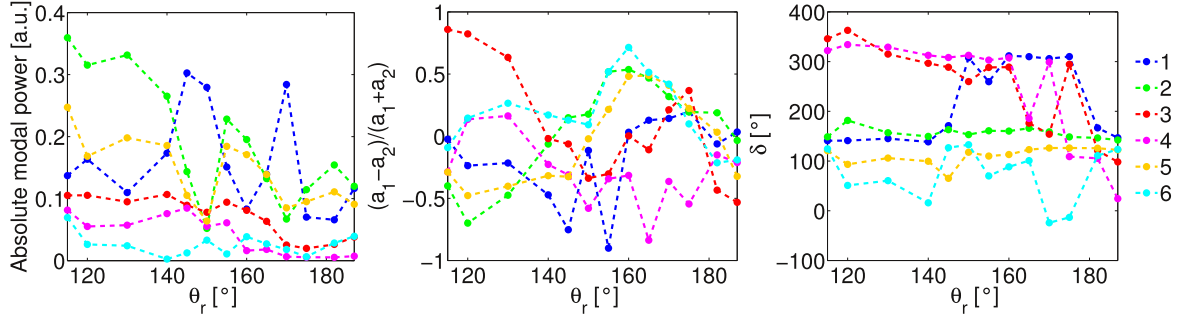
Fig. 3.14 Modal power and polarization for the modes at 780 nm as a function of the screw rotation angle θ_r: modal power (left), normalized difference of modal amplitudes (middle) and intramodal phase (right). The modal power is absolute and normalized to the initial total power.

linearly with the rotation angle[4] because the vertical shift is small (4.2 µm/1°). As evident from fig. 3.14 the modal powers of mode 1, 2 and 5 show damped oscillations. Thereby, the power oscillation of mode 1 is out of phase with mode 2 and 5 indicating intermodal power exchange. Mode 3 and 4 do not contribute to the power transfer and are attenuated more strongly at high mechanical load. Further, fig. 3.14 reveals strong power coupling between each two polarization-degenerated modes, represented by variations of $(a_1 - a_2)/(a_1 + a_2)$. Regarding the intramodal phase, it is apparent that mode 1, 2 and 5 show similar behavior as well as mode 3 and 4. While the intramodal phases of the first group are nearly independent of the vertical pressure, except for a 180°-phase jump of the fundamental mode, the intramodal phases of mode 3 and 4 slightly decrease and exhibit oscillations for increased strain. Thereby the behavior of mode 2 and 5 is quite remarkable, since a constant[5] intramodal phase implies a constant modal beat length $L_{B,l} = \lambda/B_l$ with $B_l = |n_{eff,l}^x - n_{eff,l}^y|$, and therefore a constant modal birefringence B_l. A possible explanation is, that for mode 2 and 5 n_{eff}^x and n_{eff}^y are altered in such a way, that the difference is kept constant.

The total power loss amounts to 3.9 dB which is far less than the observed power loss at bending.

3.5.3 Dependence on Input Polarization

Bending and compressing the fiber results in fiber internal stress. The polarization of the input light is an external parameter, whose variation is expected to give more reproducible results since the fiber needs not to be changed in some way.

---

[4]The tightening torque of the screw for each rotation angle is unknown and therewith the constant of proportionality.

[5]Standard deviations: 10° for mode 2 and 18° for mode 5.

To change the input polarization, the linearly polarized beam from the Nd:YAG and helium neon laser is rotated in polarization by means of a half-wave plate. A rotation of the input polarization by θ_{in} continuously redistributes the power of each two polarization-degenerated modes, i.e., the term $(a_1 - a_2)/(a_1 + a_2)$ decreases with $\Psi = 0° \ldots 90°$ and increases with $\Psi = 90° \ldots 180°$, where $a_1 \propto \cos \Psi$ and $a_2 \propto \sin \Psi$ for linearly polarized light. Neglecting fiber twist and intramodal power coupling, i.e., the proportion of a_1 and a_2 stays constant, the orientation angle of the modal polarization ellipses Ψ_l equals θ_{in}. The modal ellipticity ε_l is then expected to change as:

$$\varepsilon_l = \frac{2a_{1,l}a_{2,l}\sin\delta_l}{a_{1,l}^2 + a_{2,l}^2} = 2\cos\Psi_l\sin\Psi_l\sin\delta_l = C_l\cos\Psi_l\sin\Psi_l \tag{3.2}$$

where $C_l = 2\sin\delta_l$, and $\sin\delta_l$ is independent of Ψ_l since $\delta_l = 2\pi B_l L/\lambda$ with L the fiber length and B_l depending only on the fiber geometry and possible stress.

Fig. 3.15 illustrates the polarization of the fundamental mode depending on θ_{in}. As expected, the polarization ellipse of the fundamental mode is aligned with the input light for all θ_{in}, confirming the absence of intramodal power coupling. Further, fig. 3.15 reveals an oscillating ellipticity as described by eq. (3.2). Note that the oscillations are explained by the change of a_1 and a_2, that define the rectangle which confines the polarization ellipse (cf. fig 2.8(a) on page 17), and not by the polarization beatings itself since L is constant. A best fit of the ellipticity curve (solid black line) reveals excellent agreement with the measured values and enables the calculation of $B_0 L$:

$$B_0 L = \frac{\lambda}{2\pi}\arcsin\left(\frac{C}{2}\right). \tag{3.3}$$

From $C = 1.14$ follows $B_0 L = 5.9\,\mu\text{m}$ and with $L \approx 3\,\text{m}$, the modal birefringence of the fundamental mode is calculated to be $B_0 = 2 \times 10^{-6}$.
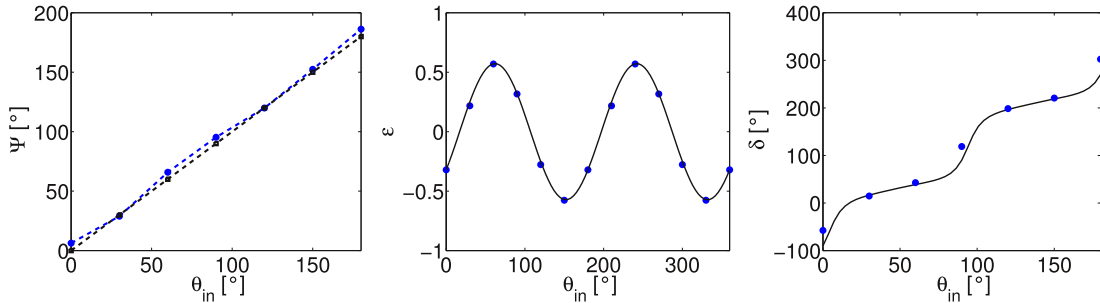

Fig. 3.15 Polarization of the fundamental mode (dashed blue lines) at 1064 nm as a function of the input polarization angle: orientation angle (left), ellipticity (middle) and intramodal phase (right). The dashed black line marks the orientation of the input polarization and the solid black lines illustrate predictions based on eq. (3.2).

Coupling linear polarized light into the fiber, aligned to the axes of birefringence, will preserve the linear polarization as indicated by the zero-crossings of ε. In the present case the zeros of ε are shifted by 17° with respect to the x- and y-axis ($\Psi = 0°$, 90°), suggesting a tilt of the axes of birefringence. Whereas in the rotated coordinate system of birefringence the intramodal phase is flat and only jumps by 180° as Ψ becomes larger than 90°, the intramodal phase becomes nonlinear in the coordinate system of analysis (x- and y-axis). To model the behavior of ε and δ in the analysis system, the modal amplitudes need to be changed to $a_{1,l} \propto \cos(\Psi_l + \Delta\Psi)$ and $a_{2,l} \propto \sin(\Psi_l + \Delta\Psi)$ with $\Delta\Psi = 17°$ as determined from the fit. With this, the intramodal phase varies as depicted in fig. 3.15, which is in good agreement with the measurement. The small deviations are caused by the variations of the output and input orientation angle.

Whereas in the single-mode regime, the dependence of ε gives information about the amount of birefringence and the orientation of its axes, the modal behavior at 633 nm is more complex, as demonstrated in fig. 3.16. Thereby, the behavior of $\Psi(\theta_{in})$, $\varepsilon(\theta_{in})$ and $\delta(\theta_{in})$ is depicted for the two bending diameters 45 cm and 5.5 cm for the first six modes. At 45 cm, the modes exhibit a large diversity regarding the orientation Ψ_l. Note that there are also some modes with opposed dependence. As in the single-mode regime at 1064 nm, the modal ellipticities are oscillating, but this time ε_l is not centered around zero for all modes, e.g., for mode 6. In fact, modes 4 and 5 are strongly elliptically polarized independent of θ_{in}.
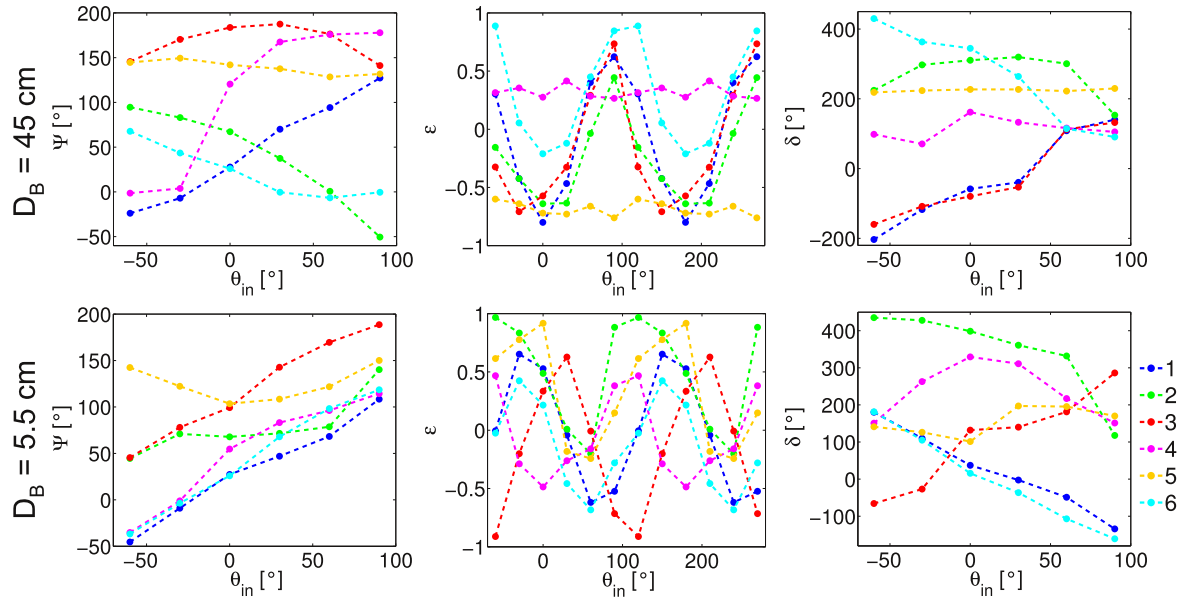

Fig. 3.16 Polarization of the first six modes at 633 nm as a function of the input polarization angle for two different bending diameters: orientation angle (left), ellipticity (middle) and intramodal phase (right).

This indicates intramodal power coupling, so that even if the input linear polarization is aligned to the axes of birefringence, this polarization state is not preserved. This means that the description with eq. (3.2) on page 35 is no longer suitable. Regarding the intramodal phase, the modal diversity is obvious, but mode 1 and 3 show similar behavior as in the experiment at 1064 nm.

For stronger bending ($D_B = 5.5$ cm), the modal diversity of Ψ_l is reduced, indicating an increased modal birefringence. The ellipticity is still oscillating, but this time the modes are phase shifted to each other, in contrast to the behavior at $D_B = 45$ cm. Further, the amplitudes and phases of ε_l are changed compared to the respective measurement at 45 cm, especially mode 4 and 5 become linearly polarized at distinct θ_{in}.

3.5.4 Dependence on Fiber Length

Monitoring the modal content and the modal polarization while cutting the fiber is an interesting approach, since it enables direct access to the modal polarization beat length and birefringence and might reveal power coupling effects.

In practice, cutting the fiber between two modal decomposition experiments is a challenging task since the adjustment of the setup needs to be retained. Further, the influence of disturbing effects such as bending must be minimized. In the experiment the setup is adjusted for the initial fiber length, and the position of the central core of the MCF, as visible in the near field intensity, is saved. The fiber is re-aligned after cutting the output facet by shifting the central core to the saved coordinates. To exclude differential influence of bending, the bending diameter was enlarged to exceed 60 cm[6]. The input facet of the fiber remains fixed while cutting the output side.

Fig. 3.17 depicts the relative modal power for excitation with the laser diode (780 nm) as a function of Δx, where $l = l_0 - \Delta x$ and l, and l_0 are the actual and initial fiber length ($l_0 \approx 3$ m). In an unperturbed fiber, the modes should propagate independently with preserved amplitudes. The apparent changes in relative modal power confirm power coupling, indicating pertubations of the modal propagation. Thereby, the total power is stable. Because of the large bending diameter and the fixation of the fiber ends with adhesive stripes, modal power changes due to macro- or microbending are excluded. Therefore, variations of fiber internal parameters, such as core diameter, pitch or refractive index along the propagation direction are probable to cause the changes in the modal power. Therefore, the measurement is an indication that the coherence of the core array is in the range of only a few centimeters. Thereby, "coherence of the array"

---

[6]A straight fiber would have necessitated the change of the position of the output coupling stage and therewith would have caused the loss of adjustment.

refers to the fact that only phase locking of the individual cores leads to the appearence of modes (supermodes), as it is the case for a perfect index structure. Pertubations may lead to phase fluctuations in individual cores yielding a redistribution of modes. The polarization beatings are not examined since the fiber could not be cleaved with smaller periods as $\approx 3\,\mathrm{cm}$.
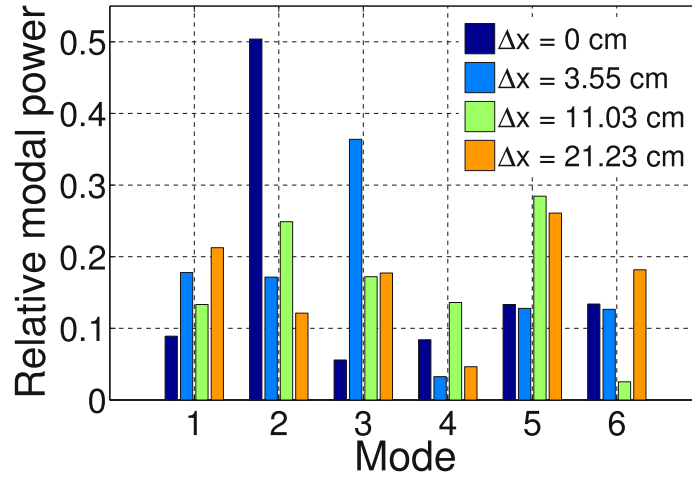

Fig. 3.17 Relative modal power as a function of the fiber length at $780\,\mathrm{nm}$.

3.6 Decomposition into Other Basis Systems

As shown in sec. 2.3.3, the field emerging from the MCF can be decomposed in an arbitrarily chosen basis set. The only requirements are the orthogonality and the completeness of the basis functions. Therefore, the modes that are implemented in the hologram need not necessarily to be the MCF modes as calculated by the mode solvers (cf. sec. 2.2). An obvious choice are the LP (linear polarized) modes that are usually used to describe mode fields of weakly guiding step-index fibers. Free space modes such as Laguerre-Gaussian (LG) or Hermite-Gaussian (HG) modes are also imaginable. However, in general it is true that the better suited the basis system, the less basis functions are needed to compose the field.

Fig. 3.18 illustrates the decomposition of a MCF beam into ten LP modes, whose overlap to the actual MCF modes is maximized (value of overlap integrals of mode $1\ldots10$ in %: $97.5\ldots92.9$). The restriction to ten modes is equivalent to a truncation of the sum in eq. (2.9) on page 13. The correlation of $93.3\,\%$ between reconstructed (fig. 3.18 (a)) and measured near field (inset in fig. 3.18 (b)) reveals good agreement and justifies the limitation to ten modes. Note that due to the truncation the high spatial frequencies in the near field intensity can not be described. The measured amplitudes
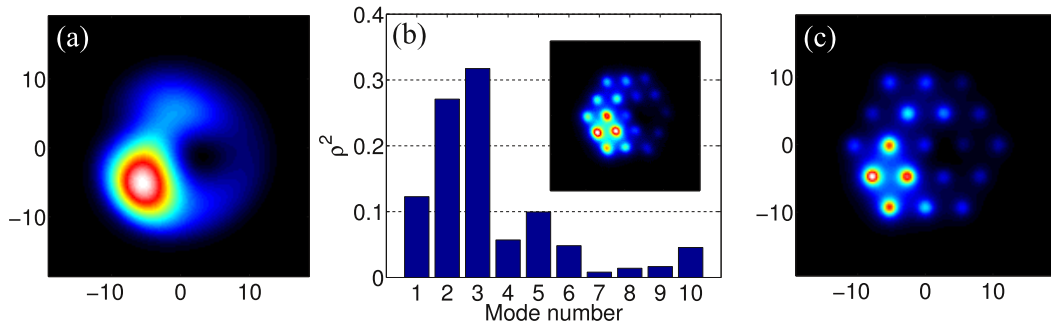
Fig. 3.18 Decomposition of MCF beam into step-index LP modes. (a) reconstruction from LP modes. (b) LP mode spectrum with measured near field intensity (inset). (c) reconstruction from MCF modes. Axes dimensions given in µm.

(fig. 3.18 (b)) and phases from the decomposition in the LP modes are also applied to reconstruct the near field intensity using the corresponding MCF modes (fig. 3.18 (c)), whose correlation to the measured intensity is excellent (96.2 %). This indicates that the truncation error is more than acceptable.

Decomposition in other basis sets is particularly attractive if only modal amplitudes are of interest, or if fast analysis is required. Using LP modes, or the mentioned free space modes, there is no need to make use of complicated mode solvers. Instead it would be worthwhile to implement LP modes for different mode field diameters and V-parameters in holograms in stock, or to use a spatial light modulator (SLM) to iteratively adapt the basis system. In both cases the laborious fabrication of a hologram with the actual modes could be omitted, yielding a much faster and more flexible mode analysis.

3.7 Beam Quality

The beam quality, represented by the M^2 factor, is a common and simple measure to evaluate the focusability and the diffraction of a beam. These attributes are of great importance in fields of applications, such as laser material processing or laser microscopy. Therefore, this section is intended to present results of simulations and measurements regarding the beam quality of the investigated fiber, and to give suggestions on how to improve the beam quality.

3.7.1 Beam Quality of the Modes

The modulation of the modal intensity distribution determines the diffraction of a mode in free space. The stronger the intensity is modulated, the higher the M^2 factor [45]. Therefore, there is the trend of increasing M^2 with ascending mode number, as depicted

in fig. 3.19(a) for the modes at 633 nm. Note that the local drops in the M^2 factor are caused by the fact that the modes are sorted by the effective indices and not by the number of intensity lobes (cf. fig. 2.3 on page 9).

Analogously, reducing the wavelength yields an increase of the M^2 value of the respective mode at this wavelength, as demonstrated in fig. 3.19(b). This is explained by the stronger power confinement in the cores towards lower wavelengths, increasing the modulation of the intensity (cf. insets of fig. 3.19(b)).

The results of fig. 3.19 are obtained by numerically propagating the mode fields using the angular spectrum method [46]. The simulated intensity patterns at discrete points in z are used to simulate a virtual caustic measurement, based on the determination of the moments of the beam, and conform to the ISO-standard [47].
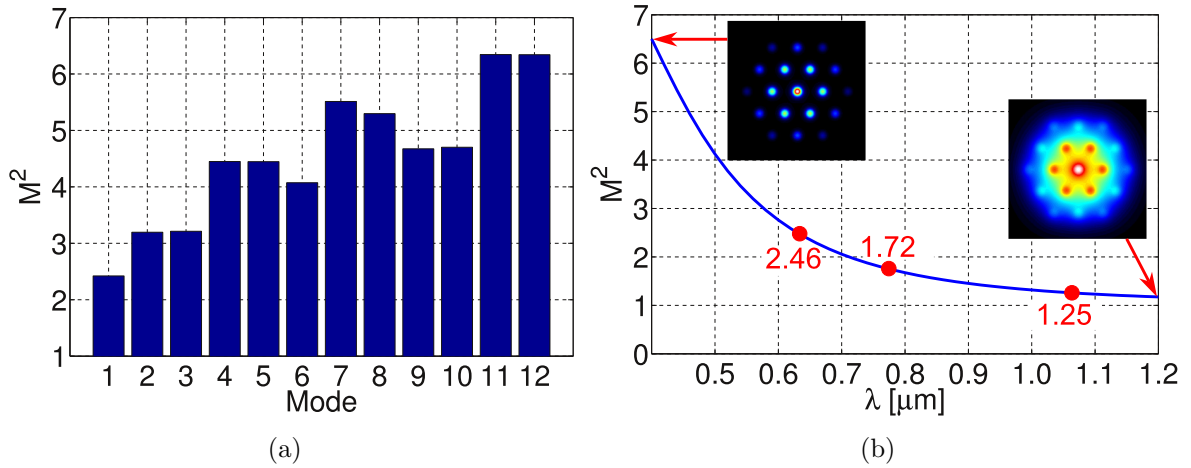

(a) (b)

Fig. 3.19 (a) M^2 factor of the modes at 633 nm. (b) M^2 factor of the respective fundamental modes as a function of the wavelength. The insets depict the modal intensity at 400 nm and 1200 nm. The M^2 values at the investigated wavelengths are marked with red points.

3.7.2 Comparison of CGH and ISO Measurement

Based on the considerations of sec. 3.7.1 it is possible to determine the M^2 factor of real mode mixtures, using the ability of the CGH-technique to completely reconstruct the field, and the virtual caustic measurement. For direct measurement, the branch of the near field recording (CCD_1 in fig. 3.1 on page 20) is extended by an additional lens to ensure ISO-conformity. Further, the polarizer is removed.

The results of the CGH-based M^2 determination are compared to direct caustic measurements in tab. 3.1 for five different mode mixtures. Whereas the results of both techniques at 633 nm are in good agreement, there is a larger relative discrepancy

λ [nm]	M^2(ISO)	M^2(CGH)	ΔM^2 [%]	dominant modes n(x %)
1064	1.16	1.26	9	1(98)
633	2.46	2.52	3	1(67), 2(11), 3(7)
	3.07	3.09	1	1(29), 2(26), 3(28)
	3.12	3.19	3	1(12), 2(15), 3(45), 4(10), 5(12)
	3.71	3.99	7	2(25), 4(27), 5(34)

Tab. 3.1 Comparison of the M^2 factor determined by direct caustic measurement (ISO) and by complete field reconstruction (CGH).

regarding the results at 1064 nm. Considering the M^2 of the fundamental mode at 1064 nm, marked in fig. 3.19(b), the result obtained by direct caustic measurement is too small. This is caused by beam clipping due to small apertures, as they are constituted by the beam splitter. At 633 nm, the effect is less critical since the smaller wavelength causes a lower diffractive spread of the high spatial frequencies with significant power as seen in fig. 3.20. Thereby the larger M^2 factor at 633 nm with respect to 1064 nm, e.g., of the fundamental mode, is caused by the the higher power fraction propagating off axis (cf. fig. 3.20). The tendency of larger M^2 obtained by the CGH-technique are explained by seeming HOMs which occur due to the background of the CCD (cf. sec. 3.9).

Whereas the uncertainty of the direct caustic measurement amounts to 0.05, the uncertainty of the CGH-measurement depends on the reconstruction quality (cf. sec. 3.9).
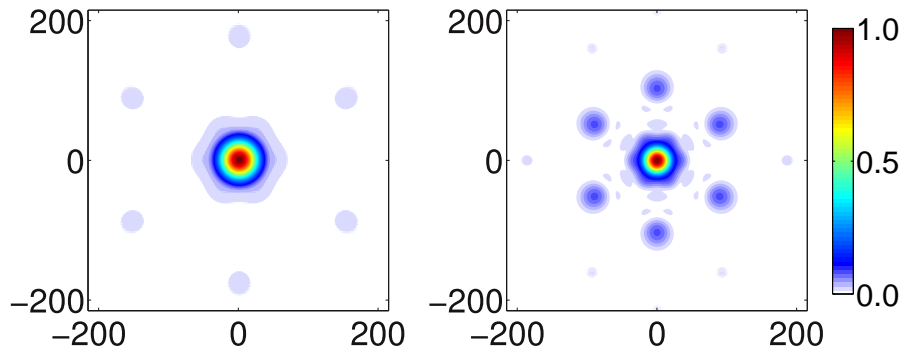

Fig. 3.20 Normalized absolute value of the field of the fundamental mode at 1064 nm (left) and 633 nm (right) after propagation of 800 µm in free space. The high spatial frequency components are clearly seen to spread off axis (axes in µm).

3.7.3 Methods Enhancing the Beam Quality

Concerning the beam quality, it is obvious from fig. 3.19 on page 40 that even the fundamental mode of the MCF, especially at 633 nm, is far away from a Gaussian beam with $M^2 = 1$. Therefore it might be interesting to further reduce the M^2 factor of beams emerging from MCFs to enhance the attractivity of the fiber for certain applications. Three different possibilities are suggested in the following.

As demonstrated in sec. 3.5.1, bending the fiber yields an increasing power fraction of the fundamental mode. This effect is tantamount to an increased beam quality with stronger bending. Reducing the bending diameter from 30 cm to 7 cm, lowers the M^2 value from 3.83 to 2.72 in the experiment of fig. 3.11 on page 31. The drawback of this method is the already mentioned total power loss (cf. sec. 3.5.1).

A possibility that avoids this disadvantage is represented by Fourier filtering. Thereby, the off axis propagating high spatial frequencies, as seen in fig. 3.20 as six hexagonally arranged field lobes, are blocked by an aperture acting as a lowpass filter. To demonstrate the effect of the method, the integration area in the evaluation of the caustic measurement is appropriately chosen, yielding a reduction of the M^2 from 2.46 to 1.40 for the second sample beam of tab. 3.1. A *physical* aperture could be used in the form of an apodized absorption filter. At 1064 nm, a M^2 reduction from 1.25 to 1.01 is possible due to simulations. The impact of filtering on the M^2 is considered by [48] for photonic crystal fibers, but is far more effective for MCFs.

An opportunity that goes along without power loss and beam manipulation is the excitation of distinct mode mixtures. Due to intermodal interferences the M^2 of a mode mixture can be smaller than that of the fundamental mode. A simple example for this is the superposition of the fundamental mode and mode 6. With the appropriate phase difference of 0 or π, depending on the definition of the phase of the modes, and an optimized power ratio, the outer ring of cores of mode 6 is out of phase with mode 1, leading to destructive interference. The superposition of those modes yields an M^2 of 1.79 at 633 nm. However, the superposition in proper phase relation requires a precise adjustment of the fiber length, which might be laborious if the modal beat length is in the order of millimeters or less.

3.8 Talbot Effect

For any periodic structure there exists a self-imaging phenomenon called Talbot imaging or Talbot effect [46]. One outcome of the effect is the reproduction of an initial intensity distribution after a distance z_T, where z_T is the so-called Talbot length, which

depends on the type of the periodic structure.

The Talbot length for an infinitely extended hexagonal pattern of period Λ is $z_T = 1.5\,\Lambda^2/\lambda$ [49]. With $\Lambda = 5.5\,\mu m$, z_T becomes $42.6\,\mu m$ at $1064\,nm$, and $71.7\,\mu m$ at $633\,nm$. Moving the end facet of the fiber in z-direction with the nano-positioning unit, and recording the near field intensity with a CCD at $633\,nm$, the reproduction of the initial intensity distribution of a mode mixture with high fundamental mode content can be observed at a translation of $70\,\mu m$, as seen in fig. 3.21. This value is in good agreement with the theoretical prediction. Further, an inverse structure is measured at half the Talbot distance (cf. fig. 3.21). The wavelength of $633\,nm$ is used in the experiment since it provides the best resolution of the near field. Note that the correlation between the intensity distributions at $z = 0$ and $z = z_T$ is detected by eye. To introduce a more quantitative criterion of comparison, the propagation of individual modes is simulated (cf. sec. 3.7.1), and the correlation is evaluated using the correlation coefficient as defined in [35]. Doing so, mode 1 reproduces its intensity distribution after $z = 41.7\,\mu m$ with $99.5\,\%$ correlation at $1064\,nm$, and after $z = 71.8\,\mu m$ with $96.8\,\%$ correlation at $633\,nm$. For ascending mode number the Talbot length increases whereas the correlation drops. This is refered to the complex phase and amplitude structure of the HOMs and depicts an important issue for mode selection. For example, this property is exploited to select the fundamental mode in MCF lasers in so-called Talbot cavities [8].
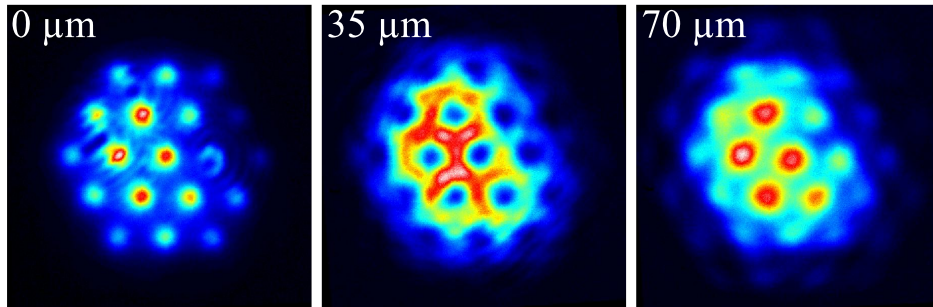

Fig. 3.21 Measured beam intensity of a mode mixture with high content of fundamental mode ($633\,nm$) at various distances from the near field plane ($z = 0\,\mu m$).

3.9 Uncertainty Considerations

This section is intended to name possible sources of errors and to make suggestions on how to avoid them. Thereby, it is out of the scope of this work to qualitatively describe the origin and evolution of errors in detail.

One of the main experimental challenges may be the correct adjustment of the CGH

with respect to the object of investigation, and to find the local optical axes that define the grid of pixels at which the intensity is measured (correlation answers). This is usually done by illumination with a symmetric intensity distribution at the examination wavelength as provided by single modes. Especially HOMs are suitable for this case since they exhibit very narrow intensity peaks in their correlation answers. But exciting single modes to a high fraction ($> 95\,\%$) is often laborious and mostly possible only for the fundamental mode, e.g., by bending. A fraction of other modes will lead to shifted grid coordinates and therewith to wrong modal amplitudes and phases. However, recent studies revealed that a broadband source is well suited to find the correct coordinates since it provides uniformly shining cores. If the hologram is illuminated with a symmetric intensity distribution, the CGH can be transversally adjusted according to the symmetry of the correlation answers. In z-direction, the CGH is placed at the position of the beam waist with a flat phase. Thereby, a transverse or longitudinal shift of the CGH, a deviation from the beam radius the CGH is designed for, and aberrations of the lenses will lead to wrong correlation answers. Uncertainties of the focal lengths of the lenses, especially at different wavelengths, and of the fiber geometry are possible sources of error regarding the beam radius.

Another critical point is the background of the diffraction pattern as caused by camera noise and light scattering from the CGH and from inhomogeneities and impurities of the lenses and optical filters. In the case of the Nd:YAG laser, also pump light might contribute to the background. The background leads to non-vanishing correlation answers of modes that are in fact not contained in the mode mixture. The CCD background, regarding the modal amplitudes, is $1\,\%$ per mode channel as determined from the seeming amplitudes of mode 2 and 3 at $1064\,\text{nm}$.

To measure the polarization of the field, a quarter-wave plate and a rotatable polarizer are necessary (cf. fig. 3.1 on page 20). The rotation of the polarizer deflects the beam, so that the CGH may be adjusted for a certain rotation angle, and is out of adjustment for another. The resulting beam pointing instability was minimized by shortening of the path length from polarizer to CGH ($25\,\text{cm}$) and to adjust the CGH for a rotation angle in the middle of the measurement range. The main part of the deflection is caused by non-perpendicular incidence on the polarizer leading to a maximal shift of 10 pixels, and not by the inherent deflection of 5" ($\widehat{=}\,5\,\mu\text{m}\,\widetilde{\approx}\,1$ pixel). The shift of the near field intensity can be corrected due to the visible cores, which is a crucial point for determining the Stokes parameters spatially resolved. Further, the mechanical forces acting by rotation of the polarizer necessitate a high stability of its mounting.

Transmittance and reflectance of the beam splitter depend on the rotation angle of the polarizer, which influences the determination of the local and modal polarization

as well as the intensity reconstruction and the modal spectrum. By measuring this dependence for each wavelength, this effect is easily corrected.

Polarizer and quarter-wave plate are adjusted by eye with respect to the x- and y-axis (defined by the 0° and 90° lines of the polarizer scale). To calculate the Stokes parameters as outlined by eq. (2.19) on page 18, the fast axis of the quarter-wave plate has to be oriented in y-direction. The uncertainty of alignment of polarizer and quarter-wave plate is assumed to be less than 5°, besides the uncertainty of the orientation of the real fast axis with respect to the mark on the housing of 3°.

Additionally, instabilities of the laser power affect the uncertainty of the vector beam intensity and its polarization. Whereas high frequency fluctuations are circumvented by averaging the correlation answers over many CCD frames (usually 20), slowly varying power drifts would necessitate the application of a reference detector. The uncertainty in the modal amplitude and phase from statistical reasons are estimated by measuring the fluctuations of amplitude and phase over 100 frames at 1064 nm with a saturation degree of the CCD camera ranging from 93 % to 4 %. Thereby the uncertainties vary in-between 0.4 % ... 2 % and 2° ... 6°.

Chapter Summary

The CGH-based measurement technique is used to completely characterize fields emerging from a MCF. The field reconstruction yields the beam intensity, the modal spectrum, the local polarization, the local phase and the modal polarization as demonstrated at a sample beam at 633 nm. The capabilities of the method enable the detailed investigation of modal properties as a function of parameters such as bending diameter, strain, polarization state of the excitation light, and fiber length, revealing characteristic features of the MCF.

The generality of the field decomposition principle is demonstrated by choosing an appropriate set of step-index fiber LP modes as basis set. Advantages and possible applications of this approach are outlined.

The beam quality of mode mixtures at different wavelengths is determined by numerical propagation and direct caustic measurement, yielding consistent results. The three suggested possibilities to enhance the beam quality are applicable to other fibers than MCFs as well.

Finally, the Talbot effect for MCF modes is considered yielding a self-imaging length depending on the mode number and wavelength.

4 Summary

The potential of the CGH-method is based on the precise knowledge of the mode fields of the considered structure. Therefore, the modes of the investigated multicore fiber (MCF) are calculated using different approaches, such as a scalar coupled mode theory (CMT), four different vectorial mode solvers (finite element method (FEM, COMSOL), finite difference method (FD), multipole method (MP, CUDOS), source model technique (SMT)), and an equivalent step-index model (ESI). By comparing the results to that of the FEM solver for the first six modes at $633\,\mathrm{nm}$, highest accuracy is achieved by the MP solver, regarding the effective indices (mean discrepancy 8×10^{-9}) and the mode fields (mean overlap $99.96\,\%$). In contrast to the vectorial mode solvers, the results of the CMT become inaccurate with increased wavelength, but are in good agreement with the FEM solver at $633\,\mathrm{nm}$.

Stronger coupling between individual cores causes a growing synchronization of phases and reduces the number of modes. According to calculations, twelve, six and three modes are propagating at $633\,\mathrm{nm}$, $780\,\mathrm{nm}$ and $1064\,\mathrm{nm}$, respectively. Experimentally determined numbers are seven, six and one for the corresponding wavelengths, concluded from the highest exciteable modes.

The modes are transverse in good approximation with a dominating transverse component (power of the z-component $\approx 10^{-4}$, and power of the weak transverse component $10^{-3} \ldots 10^{-9}$ of the power of the dominant transverse component), yielding a nearly complete and orthogonal set of linearly polarized modes. Thereby, each degenerated pair of linearly polarized modes can be superposed to form a set of vector modes, each vector mode having two non-vanishing field components in general. This reduced set can compose arbitrary vector fields, whose reconstruction is theoretically described by modal decomposition of its scalar components. The correct phase relation, as determined from the measurement of the Stokes parameters, completes the information about the vector field.

The field reconstruction is experimentally demonstrated at a sample beam at $633\,\mathrm{nm}$, including the determination of quantities such as beam intensity, local polarization, local phase, modal spectrum and modal polarization. Thereby, the local phase describes the position of the electric field vector on the polarization ellipse at a fixed time.

Comparing the local polarization at 633 nm to the global one in the single mode regime at 1064 nm, emphasizes this property to be a feature of multimodal beams.

Using the capability of the CGH-technique, enables to investigate the modal polarization and modal power as a function of parameters such as bending diameter, strain, input polarization, and fiber length, revealing characteristics of the MCF.

Thereby, bending enhances the relative content of the fundamental mode, as shown at a sample beam at 633 nm. Comparing the total power loss at 633 nm to the one at 1064 nm, much higher sensitivity to bending is detected at the near infrared wavelength. The variation of the input polarization at 1064 nm gives rise to a preserved orientation angle of the modal polarization ellipse and an oscillating ellipticity, which is theoretically explained yielding a modal birefringence of 2×10^{-6}. Whereas at 633 nm the orientation angle is not preserved at a bending diameter of 45 cm, stronger bending to 5.5 cm enhances the correlation between input and output polarization direction, indicating an increased birefringence. Further, intermodal as well as intramodal power coupling could be demonstrated while bending and straining the fiber, or by varying the fiber length. Thereby, the last mentioned effect suggests a coherence loss of the core array within few centimeters.

The generality of the field decomposition principle is demonstrated by choosing an appropriate set of step-index fiber LP (linearly polarized) modes as basis set. Advantages and possible applications of this approach are a faster and more flexible modal analysis, enabling the characterization of unknown fiber structures.

Determining the beam quality of mode mixtures at different wavelengths by numerical propagation as well as direct caustic measurement, yields consistent results with deviations smaller than 10 %, regarding the M^2 value. Three possibilities are discussed to enhance the beam quality, such as Fourier filtering, fiber bending, and modal superposition, reducing the M^2 factor for the considered examples as far as 57 %, 71 % and 73 % of the initial value, respectively.

The self-imaging length of the modes is measured and simulated, and compared to analytical results, revealing agreement for the fundamental mode. Higher order modes (HOMs) reproduce their intensity distributions in larger distances, which is essential for mode selection in Talbot cavities of MCF lasers.

Finally, the uncertainties of modal amplitudes and phases on the one hand, and of the polarization on the other, are considered as well as their sources. Future investigations are necessary to estimate those uncertainties in detail, to improve the adjustment of the CGH and of the polarization analyzing elements, and to establish an efficient background correction with the aim of an increased measurement accuracy.

Further, investigations concerning the mutual coherence of the modes as a function of

the fiber length would be of interest. In fact, the coherence length of the laser is known, but statistical fluctuations in the fiber geometry or refractive index may destroy locked phase relations. Thereby, the CGH may additionally be used to measure the degree of coherence. Regarding the array of cores, this subject depicts especially for MCFs an interesting field of research.

Another issue is the extension of the real-time ability of the CGH-technique. Indeed, the modal decomposition of a scalar field is currently done with $7.5\,$Hz, but the modal content and polarization of the entire vector beam, whose measurement presently takes several minutes, should be on hand with the same measurement rate. The application of an automatized rotating quarter-wave plate or the use of several polarizers may constitute possible solutions. Real-time recording of modal content and polarization would actually increase the understanding of the processes taking place within the fiber, and boost the attractivity of the CGH-technique for an even larger field of applications.

Bibliography

[1] F. Mitschke, *Glasfasern - Physik und Technologie* (Spektrum Akademischer Verlag, 2005).

[2] P. K. Cheo, G. G. King, and Y. Huo, Proc. SPIE **5335**, 106 (2004).

[3] B. M. Shalaby, V. Kermene, D. Pagnoux, A. Desfarges-Berthelemot, A. Barthélémy, M. A. Ahmed, A. Voss, and T. Graf, Applied Physics B: Lasers and Optics **97**, 599 (2009).

[4] M. M. Vogel, M. Abdou-Ahmed, A. Voss, and T. Graf, Opt. Lett. **34**, 2876 (2009).

[5] G. M. H. Flockhart, W. N. MacPherson, J. S. Barton, J. D. C. Jones, L. Zhang, and I. Bennion, Opt. Lett. **28**, 387 (2003).

[6] M. Koshiba, K. Saitoh, and Y. Kokubun, IEICE Electronics Express **6**, 98 (2009).

[7] N. Elkin, A. Napartovich, V. Troshchieva, and D. Vysotsky, Optics Communications **277**, 390 (2007).

[8] Y. Huo and P. Cheo, J. Opt. Soc. Am. B **22**, 2345 (2005).

[9] E. J. Bochove, P. K. Cheo, and G. G. King, Opt. Lett. **28**, 1200 (2003).

[10] B. Shalaby, V. Kermène, D. Pagnoux, A. Desfarges-Berthelemot, A. Barthélémy, A. Popp, M. Abdou Ahmed, A. Voss, and T. Graf, Applied Physics B: Lasers and Optics **100**, 859 (2010).

[11] M. Fridman, G. Machavariani, N. Davidson, and A. A. Friesem, Applied Physics Letters **93**, 191104 (2008).

[12] M. Meier, V. Romano, and T. Feurer, Applied Physics A: Materials Science & Processing **86**, 329 (2007).

[13] R. Dorn, S. Quabis, and G. Leuchs, Phys. Rev. Lett. **91**, 233901 (2003).

[14] H. G. Berry, G. Gabrielse, and A. E. Livingston, Appl. Opt. **16**, 3200 (1977).

[15] H. Laabs, B. Eppich, and H. Weber, J. Opt. Soc. Am. A **19**, 497 (2002).

[16] O. Shapira, A. F. Abouraddy, J. D. Joannopoulos, and Y. Fink, Phys. Rev. Let. **94**, 143902 (2005).

[17] N. Andermahr, T. Theeg, and C. Fallnich, Appl. Phys. B **91**, 353 (2008).

[18] Y. Z. Ma, Y. Sych, G. Onishchukov, S. Ramachandran, U. Peschel, B. Schmauss, and G. Leuchs, Applied Physics B: Lasers and Optics **96**, 345 (2009).

[19] J. W. Nicholson, A. D. Yablon, S. Ramachandran, and S. Ghalmi, Opt. Express **16**, 7233 (2008).

[20] Z. Pu, W. Xiao-Lin, M. Yan-Xing, M. Hao-Tong, X. Xiao-Jun, and L. Ze-Jin, Chinese Physics Letters **26**, 084205 (2009).

[21] M. Wrage, P. Glas, M. Leitner, T. Sandrock, N. N. Elkin, A. P. Napartovich, and A. G. Sukharev, Optics Communications **175**, 97 (2000).

[22] A. Yariv, *Optical Electronics in Modern Communications* (Oxford University Press, 1997).

[23] A. S. Kurkov, S. A. Babin, I. A. Lobach, and S. I. Kablukov, Opt. Lett. **33**, 61 (2008).

[24] Y. Huo, P. Cheo, and G. King, Opt. Express **12**, 6230 (2004).

[25] P. S. Russell, J. Lightwave Technol. **24**, 4729 (2006).

[26] A. Fallahkhair, K. S. Li, and T. E. Murphy, J. Lightwave Technol. **26**, 1423 (2008).

[27] Z. Zhu and T. Brown, Opt. Express **10**, 853 (2002).

[28] H. Uranus and H. Hoekstra, Opt. Express **12**, 2795 (2004).

[29] A. Hochman and Y. Leviatan, Opt. Express **15**, 14431 (2007).

[30] T. P. White, B. T. Kuhlmey, R. C. McPhedran, D. Maystre, G. Renversez, C. M. de Sterke, and L. C. Botten, J. Opt. Soc. Am. B **19**, 2322 (2002).

[31] B. T. Kuhlmey, T. P. White, G. Renversez, D. Maystre, L. C. Botten, C. M. de Sterke, and R. C. McPhedran, J. Opt. Soc. Am. B **19**, 2331 (2002).

[32] S. Campbell, R. C. McPhedran, C. M. de Sterke, and L. C. Botten, J. Opt. Soc. Am. B **21**, 1919 (2004).

[33] G. Canat, R. Spittel, S. Jetschke, L. Lombard, and P. Bourdon, Opt. Express **18**, 4644 (2010).

[34] A. W. Snyder and J. D. Love, *Optical Waveguide Theory* (Chapman & Hall, 1996).

[35] D. Flamm, "Analysis of cylindrical vector beams emerging from passive LMA-fibers by means of holographic filters", Diploma thesis, Friedrich-Schiller-Universität Jena (2009).

[36] M. Born and E. Wolf, *Principles of Optics* (Pergamon Press, 1991).

[37] W.-H. Lee, Appl. Opt. **18**, 3661 (1979).

[38] R. Schermer and J. Cole, Quantum Electronics, IEEE Journal of **43**, 899 (2007).

[39] D. Marcuse, J. Opt. Soc. Am. **66**, 311 (1976).

[40] J. P. Koplow, D. A. V. Kliner, and L. Goldberg, Opt. Lett. **25**, 442 (2000).

[41] A. M. Smith, Appl. Opt. **19**, 2606 (1980).

[42] A. Harris and P. Castle, Lightwave Technology, Journal of **4**, 34 (1986).

[43] I. Kaminow, Quantum Electronics, IEEE Journal of **17**, 15 (1981).

[44] K. Okamoto, T. Hosaka, and T. Edahiro, Quantum Electronics, IEEE Journal of **17**, 2123 (1981).

[45] B. Neubert and B. Eppich, Optics Communications **250**, 241 (2005).

[46] J. W. Goodman, *Introduction to Fourier Optics* (McGraw-Hill, 1968).

[47] ISO, "11146-2:2005 Test methods for laser beam widths, divergence angles and beam propagation ratios – Part 2: General astigmatic beams", (2005).

[48] J. Shephard, P. Roberts, J. Jones, J. Knight, and D. Hand, Lightwave Technology, Journal of **24**, 3761 (2006).

[49] J. T. Winthrop and C. R. Worthington, J. Opt. Soc. Am. **55**, 373 (1965).

Acknowledgements

Erklärung

Ich versichere hiermit, dass ich die vorliegende Diplomarbeit selbständig verfasst, keine anderen als die angegebenen Quellen und Hilfsmittel verwendet, sowie Zitate kenntlich gemacht habe.

_____   _____
Ort, Datum   Unterschrift

Seitens des Verfassers bestehen keine Einwände, die vorliegende Diplomarbeit für die öffentliche Nutzung in der Thüringer Universitäts- und Landesbibliothek zur Verfügung zu stellen.

_____   _____
Ort, Datum   Unterschrift